UNIVERSITY OF COPENHAGEN
DEPARTMENT OF GEOSCIENCES AND NATURAL RESOURCE MANAGEMENT

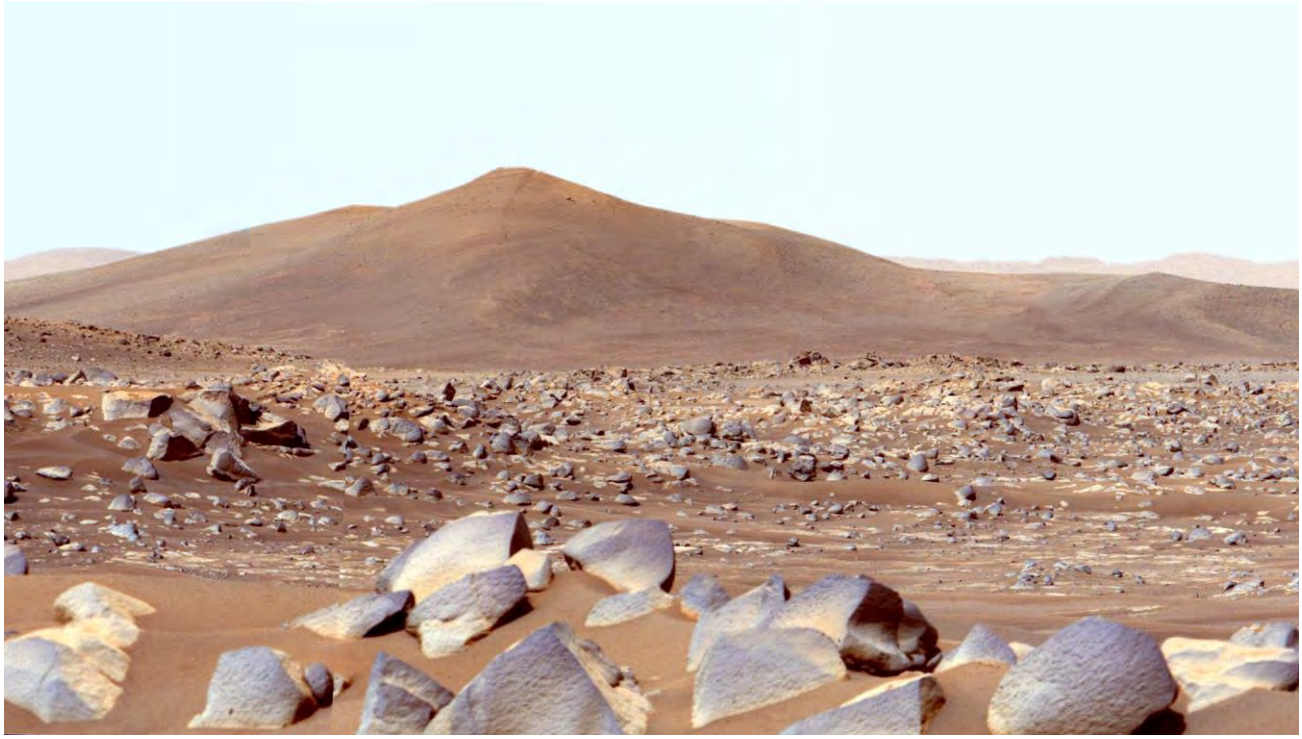

Stratigraphy and origin of geologic units in Jezero crater, Mars

Michael D. Hansen

60 ECTS

Supervisor: Kjartan M. Kinch

Submitted on: November 30, 2021

Acknowledgements

First and foremost, I would like to thank my primary supervisor, Kjartan M. Kinch for his immense support throughout the process of writing this thesis. His encouragement in the Mars 2020 mission has been very contagious, and I am very grateful for him (and Dr. Jim Bell) for taking me into the Mastcam-Z team. My time in the Mastcam-Z team has taught me so much about Mars rover operations, and I have never felt that my opinion was less valued despite being a student. I would like to thank everyone in the Mastcam-Z team and the M2020 team for countless educational hours while working together.

I would also like to thank Dr. Sanna Holm-Alwmark for being the primary author of a paper including some of my work presented in this thesis. Also, Sanna has shown great enthusiasm about my project and provided me with constructive feedback.

Furthermore, I want to thank my co-supervisor, Kristian Svennevig, for his (much needed) GIS support in the early stages of this thesis, as well as his constructive feedback during the final stages.

Lastly, I would like to express my gratitude to my family and my friends for their immense support and encouragement throughout the entire process of writing this thesis. I am forever grateful for what they (and everyone above) have done for me.

Michael D. Hansen – jbt620
November 30, 2021
University of Copenhagen

Abstract

Jezero crater is a ~45 km diameter impact crater located on the northwestern edge of the Isidis Basin on Mars. Within the crater is an assemblage of geologic units. The stratigraphic ordering of this assemblage has been debated for several years, and the debate has intensified since Jezero crater was selected as the landing site for NASA's Mars 2020 Perseverance rover mission, and since the rover landed on February 18, 2021.

In this thesis I investigate orbital data (HiRISE images and associated digital elevation models (DEMs)), to assess the stratigraphic relations in Jezero crater. I have created topographic profiles and a map based on DEMs to investigate unit boundaries. The topographic profiles are based on some of my previous work included in my Bachelor's project, and was reworked and refined to reach a standard for publication in Holm-Alwmark et al., 2021.

Additionally, some of my work as part of the Mastcam-Z downlink science support team is presented and discussed, in an attempt to associate rock morphotypes and regolith to source units within Jezero crater. A more detailed classification of the geologic units present in Jezero crater, is crucial for understanding evolution of the fluviolacustrine system and determining the potential habitable environments within the crater.

My results presented in this thesis are unambiguous in constraining the relative timing of events in Jezero crater and determining the origin of geologic units. The types of unit boundaries (i.e., with or without local depressions) observed through orbital and rover data are only indicative of the relative timing of deposition. Future investigations by the Perseverance rover and the sample return mission should provide sufficient data to conclude on the stratigraphic relations in Jezero crater.

As of November 2021 (9 months after landing) the Perseverance rover is still on-going providing us with continuous scientific data. So far, the data is constrained to the crater floor in the proximity of the landing site. There are still plenty of scientific targets (i.e., craters, unit boundaries, and delta deposits) in Jezero crater to be investigated which may reveal key factors in constraining the relative timing of events in the crater.

Table of contents

1. Introduction

The geological history of the crust of Mars includes processes such as impact basin formation, igneous petrogenesis, climate evolution, and ancient aqueous environments that are essential for understanding the origin, early evolution, and habitability of terrestrial planets. In November 2020, the United States National Aeronautics and Space Administration (NASA) launched the most recent Mars rover mission, Perseverance. The rover touched down in Jezero crater on February 18, 2021, and acts as the first step in collecting and returning samples to Earth. Jezero crater holds evidence of a prolonged history of lacustrine activity within the crater, with the presence of inlet and outlet channels, as well as the preservation of a fluvial delta near the western margin of the crater. Understanding the timing and relationships between units present within Jezero crater is crucial to understanding the hydrological processes and geologic history of the Nili Fossae region and with broader implications for the entire planet.

The aim of this study is to assess the stratigraphic relations between the geologic units within the crater, and to associate rock and regolith observations made by the Perseverance rover with these geologic units. Delta-associated remnant deposits within the crater are also investigated, to try to determine whether they are of deltaic or lacustrine origin. Some of the work presented in this thesis was made as contribution to Holm-Alwmark et al., 2021.

Initially this thesis presents a historic overview of Mars exploration performed by NASA (Section 2), leading up to the most recent Mars 2020 (M2020) Perseverance rover mission. Following is Section 3 on the background and geological setting of Jezero crater, including descriptions of the geologic units present within the crater. The methods, data, and results presented in Sections 4, 5, and 6, are subdivided into orbital data and in-flight (rover) data for convenience, as data collection for this thesis was made both prior to and after the M2020 landing. Following is a discussion (Section 7) on the outcomes of the results included in this study, along with a conclusion (Section 8) on the most fundamental observations made. As the thesis is based on data provided by a currently active rover mission, the presented data has been acquired continuously since February 2021.

2. Mars exploration

2.1 Chronology of Mars exploration

Some of the first known documentation of Mars observation date back to the ancient Egyptians at approximately 2.000-1.000 BC. Naturally the Egyptians did not know all about the planets that we do now. At the time only five planets were known: Mercury, Venus, Mars, Jupiter, and Saturn – all orbiting Earth according to the geocentric model. They had good knowledge of their positions in the sky, their color and brightness, as well as the retrograde motion of Mars (Novaković, 2008).

The 16th century revolutionized our view of the universe, when Nicolaus Copernicus proposed the heliocentric model, with the Sun being the principal body in the universe. The heliocentric model was naturally met with skepticism and resistance, but with the support of Galileo Galilei and Johannes Kepler, it eventually superseded the geocentric model (Westman, 2001). Much of the astronomical observations, that Kepler used to prove the heliocentric model were collected by Tycho Brahe, who took Kepler on as his assistant. At the time, Brahe had his own Earth-centered model of the Universe and withheld most of his observations from Kepler to prevent him from proving the heliocentric model. It was only after the death of Brahe, that Kepler proved heliocentrism and calculated the orbital laws, using Brahe's astronomical observations (NASA EO, 2009). The first telescopic observations of Mars happened in 1609 by the telescope of Galileo Galilei. Until Galilei's telescope only the position in the sky was known about Mars, as the angular size is simply too small for the naked eye to resolve. The invention and still ongoing development of the telescope allowed for observations of surface features of Mars, as well as other celestial bodies in the Solar System, over the following centuries (Harland, 2005).

In the 1960s the space exploration programs began with the developments in ballistic missile capabilities. The 1960s Mars exploration programs consisted of a series of flyby missions, until eventually orbiters were launched towards the red planet in the early 1970s (Garber, 2015).

2.2 NASAs historic surface exploration

Since the mid-1970s, NASA has launched a series of missions to the surface of Mars. Through decades of Mars exploration, most of NASAs landers and rovers have inherited designs and technologies directly from previous missions. It is a feasible strategy to send technology that is known to work as intended on Mars, to lower the risk of component failure. Not only have the landers and rovers gone through physical evolution, the communication processes during both tactical and strategic operations have developed over the past decades. One example being, as a Martian day (a sol) is 24 hours and 39 minutes, planning for rover operations during the Martian daytime is not as simple as it may sound. For efficiency, most of the recent Mars rover missions have worked according to Mars time for the first 3 months of operations, and then transitioned into a regular Earth schedule. This transition to working according to Earth time, leads to sols with none or restricted planning and will in turn lower the efficiency of rover planning (Gaines et al., 2016). On the most recent mission, the Mars 2020 mission, a quite refined system for rover planning is in place to maximize efficiency on sols with none or restricted planning. This includes operational shifts on restricted sols and planning multiple sols ahead.

Viking

The Viking program consisted of two spacecraft, Viking 1 and 2, which were based on the design of the Mariner 8 and 9 orbiters, only this time they also carried landers. The spacecraft were launched in 1975 and on July 21, 1976 we received the first image from the surface of Mars (Garber, 2015). The Viking program marks the beginning of NASAs more than 40-year long search for evidence for Martian microbial life. Although the Viking missions did not provide convincing evidence of microbial life, the program developed datasets describing the surface geomorphology and atmospheric conditions both globally and locally (Garvin & McCleese, 2003). The Viking program provided detailed color panoramic images of the Martian terrain, monitored atmospheric variations, and acquired over 52.000 images from orbit until the mission finally ended in 1983 (Garber, 2015).

Mars Pathfinder

Mars Pathfinder was the first NASA rover mission to touch down on Mars on July 4, 1997. It consisted of a base station and a roving probe named Sojourner. The Pathfinder mission returned

significant volumes of scientific data in the 3 months of surface operations at Ares Vallis. Sojourner was the first Mars rover to carry a chemical analysis instrument to characterize the rocks and soils around the landing area. The primary mission objective was to prove the development of spacecraft could be made faster, cheaper, and better. Relative to the previous Viking spacecraft, the Pathfinder spacecraft was very low-cost and paved the way for cost-effective implementation of future Mars rover missions (Golombek, 1997). The rover mission was only planned to last for a week to a month, but Sojourner managed to operate for almost 3 months until communications finally failed on October 7, 1997. A clear analogy can be drawn from this first rover mission to the more recent M2020 mission (Section 2.3), with the Perseverance rover carrying a helicopter (Ingenuity) to demonstrate powered flight by an aircraft on a planet other than Earth is possible.

Mars Exploration Rovers

The Mars Exploration Rovers (MER) named Spirit and Opportunity landed on Mars in January 2004. The MERs were the first successful rovers to land on Mars as part of NASAs Mars Exploration Program (MEP). The MEP is a long-term program with the goal of exploring the possibilities of past and/or present microbial life on Mars, and in turn prepare for human exploration, as well as assessing the climate and geology of the planet. With far greater mobility than Sojourner the rovers collected immense amounts of geological and atmospheric data. The scientific goal of the mission was to search for and characterize a wide range of rocks and soils for clues to past fluvial activity on Mars. The landing sites for the rovers are located on opposite sides of the planet, both of which appeared to have been affected by liquid water in the past (NASA MER, 2019). Both rovers carried instruments for rock and soil analysis, including cameras, three different spectrometers, and a rock abrasion tool. The MER rovers were the first to be equipped with abrasion tools, allowing for scientists to peer beneath the dusty and weathered surfaces of Martian rocks. Both rovers ultimately found evidence that water factored into the history of the near surface materials of the landing sites, suggesting wet past climates that possibly could have supported microbial life (NASA MER, 2019).

Both rovers greatly exceeded their 90-day primary mission. Spirits final communication to Earth was on March 22, 2010 and the last signal from Opportunity was received on June 10, 2019.

Phoenix

The Phoenix lander was launched in August 2007, as part of the MEP and as the name suggests, it was a rebirth of discontinued project. Phoenix was derived from the Mars Surveyor Program 2001 Lander (MSP'01), that was supposed to provide in situ verification and ground truth for data obtained by the MSP'01 orbiter, more commonly known as Odyssey (Shotwell, 2005). Phoenix was targeted to land within the north circumpolar region (65N-72N), a region that data from the Gamma Ray Spectrometer (GRS) on board the Odyssey orbiter, indicate contains extremely large quantities of water ice within the regolith. The primary scientific objectives of the Phoenix lander were to investigate water in all its phases, both in the surface soil and atmosphere, and characterize the active processes shaping the northern plains (Shotwell, 2005). The lander was operational on the surface from May 25, 2008 and the last signal was received on November 2, 2008. Phoenix successfully documented the presence of pure water ice just beneath the surface of Mars.

Mars Science Laboratory

The Mars Science Laboratory (MSL) rover, Curiosity, was launched on November 26, 2011, as part of the MEP, despite being planned for launch in 2009, as multiple technical challenges led to an extension of the development phase of the project. The configuration of the rover was inherited from the Mars Pathfinder and MER design, with a mass approximately five times greater than the MERs (Welch et al., 2013). The rover carries a wide range of instruments, including 17 cameras for navigation, hazard avoidance and scientific purposes. Additionally, Curiosity also carries four spectrometers, two radiation detectors, and an environmental sensor. Curiosity touched down in Gale Crater on August 5 and is currently still operational (NASA MSL, 2021).

InSight

The InSight lander was launched on May 5, 2018, as part of the MEP, and was designed to study the deep interior of Mars, to better understand the processes that control the early planetary formation. It carries a series of instruments including a seismometer, a radiometer, a heat flow probe and a weather station. The heat flow probe and radiometer (combined HP^3 (Heat Flow and Physical Properties Package)) are designed to hammer themselves down in the soil. This avoids the influence of the Sun and allows for measuring the internal heat flow of Mars (Banerdt, 2020).

InSight touched down at Elysium Planitia on November 26, 2018 and is currently still operational. It has provided detailed seismic data on the depth and composition of the Martian crust, mantle, and core, including confirmation that the planet's center is molten (NASA InSight, 2021).

2.3 The Mars 2020 mission

The Mars 2020 spacecraft was launched on July 30, 2020, as part of the MEP and touched down in Jezero Crater on February 18, 2021. The landing site was announced by NASA on November 19, 2018, and was selected among more than 60 candidate locations (Brown, 2020). The decision was made based on the engineering constraints of the mission as well as the potential scientific yield of the location. An important deciding factor in the selection process, was to find a landing site with a desirable geologic diversity in as small and navigable area as possible (Mustard et al., 2013).

2.3.1 Mission goals

As part of the MEP the goals of the Mars 2020 mission naturally reflects the primary goals of the MEP. As directed by NASA, the M2020 mission has four specific objectives:

1) The mission should develop a scientific understanding of the geology of its landing site
2) Based on that geologic understanding, the mission should identify ancient habitable environments, locate rocks with a high probability of preserving biosignatures, and in those rocks, the rover's instruments should be used to look for potential biosignatures
3) The mission should collect and document a suite of scientifically compelling samples for possible Earth return by a future mission
4) The mission should enable future Mars exploration especially by humans, by making progress in filling strategic knowledge gaps and by demonstrating new technologies. (Farley et al., 2020)

In response to goal 3 above, the Mars 2020 mission is intended to acquire a set of scientifically selected Mars samples for later retrieval and return to Earth through the Mars Sample-Return

(MSR) mission. NASA and ESA signed a Statement of Intent in 2018 in an attempt to implement the MSR mission in a partnership between the two agencies. The MSR concept is envisioned to be made up of three flight elements, including the M2020 mission, a Sample Retrieval Lander (SRL), and the Earth Return Orbiter (ERO). Additionally, a facility for handling the returned samples is required on the ground. Fig. 1 shows the current elements, their general interfaces, and their responsible agency (Muirhead et al., 2020).

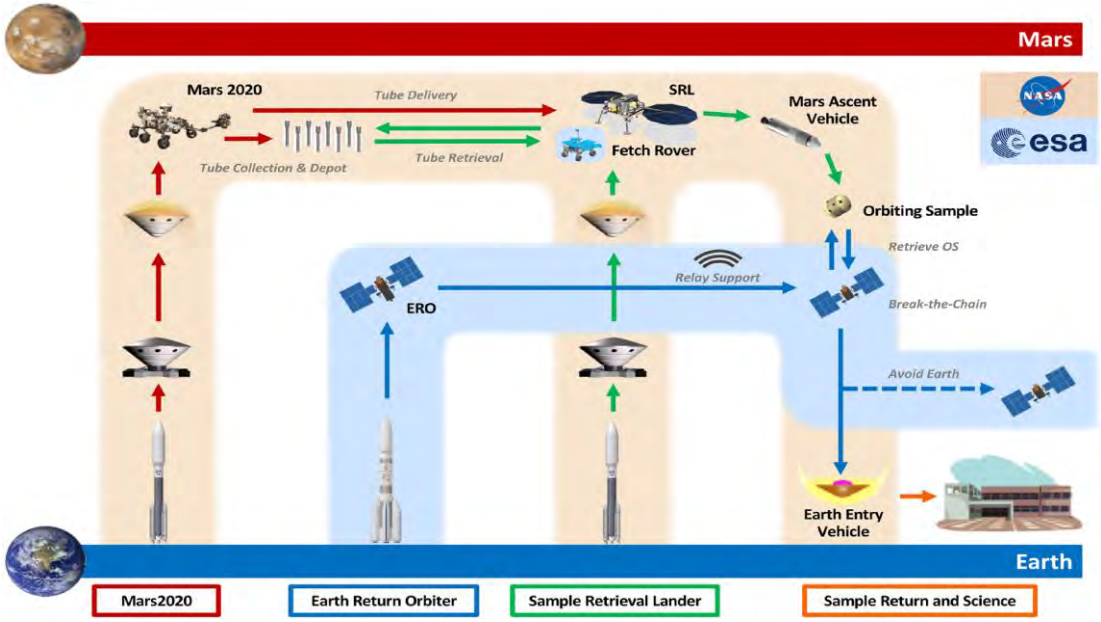

Fig. 1 – Potential joint NASA/ESA MSR campaign scenario. From: Muirhead et al., 2020

2.3.2 The Mars 2020 Rover

The design of the Mars 2020 spacecraft is based on the highly successful MSL rover, Curiosity. Not only does the rover carry a suite of cameras that are fundamentally enhanced versions of cameras on board the Curiosity rover (Williford et al., 2020), it also carries a Ground-Penetrating Radar (GPR) that will shed light on the subsurface, as well as a multi-faceted weather station for documentation of the atmospheric conditions. Two scientific sensing units are located on the Remote Sensing Mast (RSM) (Mastcam-Z and SuperCam) and two are mounted to the turret located at the end of the robotic arm (PIXL and SHERLOC) (Fig. 2). The GPR instrument, RIMFAX, is located on the underside of the rover, and the weather station (MEDA) has sensors distributed around the rover. MOXIE is an experimental instrument purposed to demonstrate production of oxygen from carbon-dioxide in preparation for human exploration of Mars. The instruments on the rover can be used both individually or in tandem to map the geologic

attributes of rocks and regolith at the meter scale and at the submillimeter scale. In order to evaluate the Martian near-surface atmosphere, Perseverance also carries a helicopter (Ingenuity) to assess the ability for rotorcraft flight in the thin Martian atmosphere (Farley et al., 2020). On April 19, 2021, Ingenuity completed the first powered flight on a planet other than Earth, and has since then performed several successful flights, proving that aerial scouting could benefit future exploration of Mars and other planets.

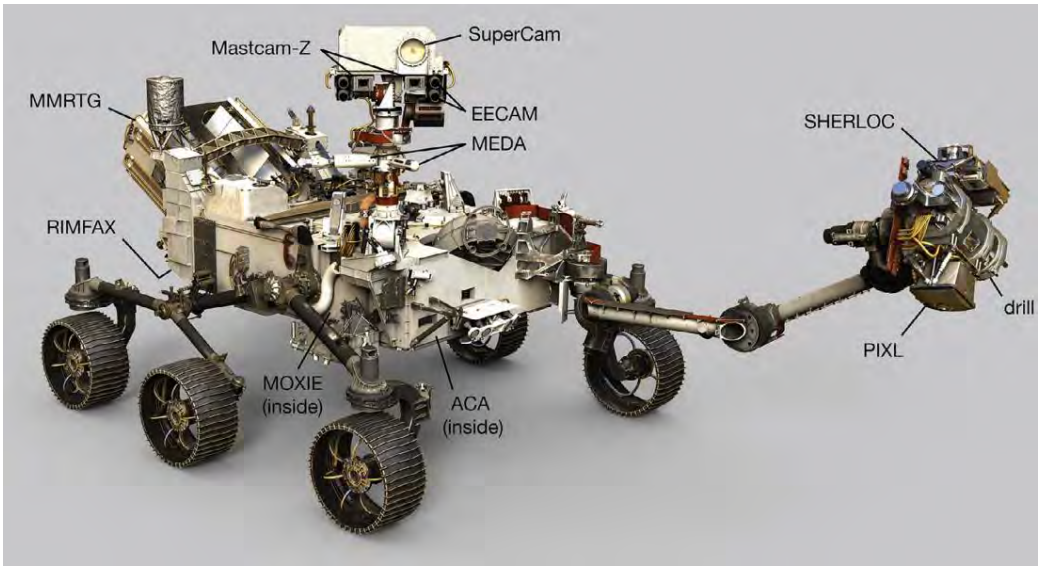

Fig. 2 - Artist's concept of the Mars 2020 rover with key elements indicated. From: Williford et al., 2020

Mastcam-Z

Mastcam-Z is, as the name implies, located on the mast of the rover. It is a pair of focusable, 4:1 zoomable 1648x1214 pixel cameras that can resolve (≥ 5 pixels across) features of ~0.7 mm at 2 m and ~3.3 cm at 100 m distance (Bell et al., 2021). The multispectral cameras can capture broadband red/green/blue (Filters 0) and narrowband imaging in 11 unique narrow bands (Filters 1-6) within the 400-1000 nm range, as well as direct solar images using neutral density filters (Filters 7) (Table 1). Because of Mastcam-Z's heritage on the MSL rover, only modest modifications were made for the enhanced Perseverance hardware implementation, such as the capability to zoom. The ability to zoom allows scientists to examine targets that would otherwise be out of reach, and view near-field rocks and regolith at a scale as small as ~133 μm/pixel at a distance of 2 m (Bell et al., 2021).

Fig. 3 - Overview of the Mastcam-Z components. (Left) Camera heads before mounting on the RSM. (Upper right) Digital Electronics Assembly (DEA) before mounting inside the rover chassis. (Lower right) Calibration targets mounted on the rover deck. For scale the pocket knife is 88.9 mm long, and the primary calibration target is 8 x 8 cm across. From: Bell et al., 2021

The Mastcam-Z hardware consists of 5 elements: two camera heads, one Digital Electronics Assembly (DEA) and two calibration targets (Fig. 3). The camera heads are mounted on the RSM (Fig. 2), the DEA within the rover chassis and the two calibration targets are mounted on top of the rover chassis. The camera heads consist of an optomechanical lens assembly (with zoom and focus actuators), a filter wheel, and a focal plane assembly and its electronics (Fig. 4). The camera heads can nominally be operated at temperatures between -40 °C and 40 °C, and have for this reason heaters attached to the outside of the camera head, to be able to thermostatically control the cameras.

The illumination condition on the Martian surface may change with time of year, time of day, and with local atmospheric conditions (such as dust loading and potential clouds). The calibration targets provide a local, instantaneous estimate of illumination conditions and allows for transformation of image data, from units of radiance (the observable) to units of reflectance (the material property), which is critically important to achieving reliable multispectral data (Kinch et al., 2020).

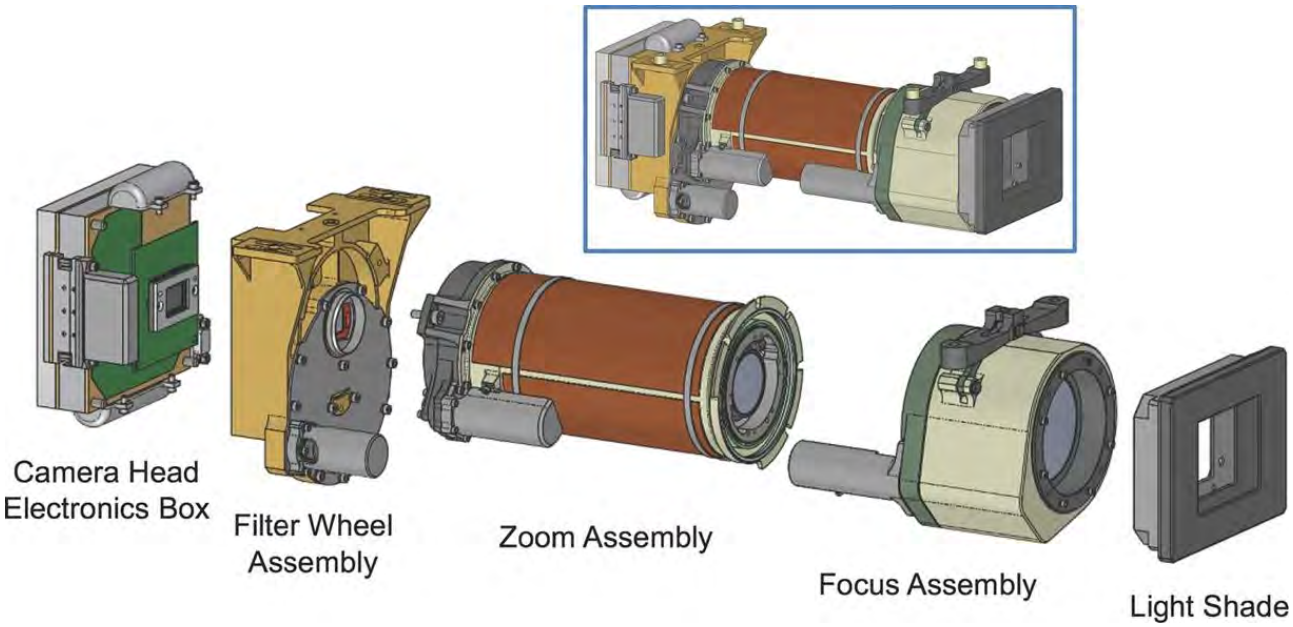

Fig. 4 - CAD model showing the Mastcam-Z optomechanical subsystems and the full camera head (blue box). From: Bell et al., 2021

Mastcam-Z Left (L) and Right (R) filters

Filter number	$\lambda_{eff} \pm$ HWHM (nm)	
L0/R0 (Red Bayer)	630 ± 43	631 ± 43
L0/R0 (Green Bayer)	544 ± 41	544 ± 42
L0/R0 (Blue Bayer)	480 ± 46	480 ± 46
L1 / R1	800 ± 9	800 ± 9
L2 / R2	754 ± 10	866 ± 10
L3 / R3	677 ± 11	910 ± 12
L4 / R4	605 ± 9	939 ± 12
L5 / R5	528 ± 11	978 ± 10
L6 / R6	442 ± 12	1022 ± 19
L7 / R7	590 ± 88	880 ± 10

Table 1 - Table showing the effective band center wavelengths of the Mastcam-Z left and right camera filters respectively. Filters in red are new additions compared to the MSL Mastcam. HWHM is the half-width of the bandpass at half-maximum for each filter. Modified table from Bell et al., 2021

The goals of the Mastcam-Z investigation respond directly to the goals of the NASA Mars 2020 mission (Section 2.3.1) and are as follows:

1. *Characterize the overall landscape geomorphology, processes, and the nature of the geologic record (mineralogy, texture, structure, and stratigraphy) at the rover field site.*
2. *Assess current atmospheric and astronomical conditions, events, and surface-atmosphere interactions and processes.*
3. *Provide operational support and scientific context for rover navigation, contact science, sample selection, extraction, and caching, as well as imaging support for other Mars 2020 instruments and rover tools.*

   (Bell et al., 2021)

Goal 1 is achieved by obtaining observations of rocks, regolith, and outcrops to determine morphology, texture, depositional or erosional history. The data will be necessary for a full description of the topography, geomorphology, geologic setting, and the nature of past and present geologic processes in Jezero Crater.

Goal 2 is achieved by observations of clouds, aerosols in suspension (dust/ice crystals), tracking of dust reposition and removal on calibration targets, astronomical phenomena, and active aeolian transport of fine sediment.

Goal 3 includes images that will provide information pertinent to rover traversability, such as distant hazards and horizon features. Additionally, this goal also includes observations assisting other Mars 2020 science instrument in determining potential materials to be collected for the MSR mission (Bell et al., 2021).

SuperCam

SuperCam is a suite of five different techniques that complement each other in determining the texture, mineralogy and chemistry of rocks remotely. The observations are made through Laser-Induced Breakdown Spectroscopy (LIBS), Time-Resolved Raman and Luminescence (TRR/L), visible and near-infrared spectroscopy (VISIR), high-resolution color imaging (RMI), and acoustic recording (MIC) (Maurice et al., 2021). The camera operates primarily at remote distances of 2-7 m, providing data at sub-mm to mm scales within that range, but RMI and VISIR are practically only limited by the atmospheric transparency or the horizon. The spectrometers of SuperCam can identify specific minerals (TRR/VISIR), major elements (LIBS) and some trace elements (TRL) within the rocks and regolith. The high-resolution RMI images complement these analyses by determining the rock type, its texture and grain size distribution (Maurice et al., 2021).

PIXL

Planetary Instrument for X-ray Lithochemistry (PIXL) is a micro-focus X-ray fluorescence (XRF) spectrometer and is one of two instruments mounted on the robotic arm. PIXL uses a powerful X-ray with a small enough diameter to analyze the chemical composition of singular grains and does so in multiple types of scans: line, grid and maps. PIXL's hyperspectral maps are approximately the size of a postage stamp and comprise 6.000-7.000 individual XRF spectra (Allwood et al., 2021). PIXL will always operate at night, as noise in the camera is very sensitive to temperature and is minimized at low temperatures. Another reason for operating at night, is because of the time required, and only few other things happening on the rover during nighttime. The small scale observations from PIXL will provide a valuable link between the larger centimeter- to meter-scale observations made by Mastcam-Z and SuperCam, and the much smaller (micron-scale) measurements made on returned samples in terrestrial laboratories after a successful sample return (Allwood et al., 2021).

SHERLOC

Accompanying PIXL on the robotic arm, is the Scanning Habitable Environments with Raman and Luminescence for Organics and Chemicals (SHERLOC) instrument. It operates with two primary boresights, one for generating spatially resolved chemical maps using fluorescence and

Raman spectroscopy coupled to microscopic images (10.1μm/pixel) and a Wide Angle Topographic Sensor for Operation and eNgineering (WATSON) that obtains color images from microscopic scales (~13μm/pixel) to infinity. Combined with observations from Mastcam-Z, PIXL and SuperCam, SHERLOC provides unprecedented analysis of the Martian rocks and regolith (Bhartia et al., 2021).

RIMFAX

RIMFAX is a ground-penetrating radar that provides the capability to image the shallow subsurface beneath the rover as it traverses Jezero Crater. RIMFAX is a Frequency Modulated Continuous Wave (FMCW) radar which operates at frequencies from 150 – 1200 MHz. FMCW radars transmits signals across a range of frequencies rather than using a single frequency, effectively increasing the signal to noise ratio. Imaging the subsurface will provide information about its composition and will aid in the selection of scientifically valuable samples for MSR. (Hamran et al., 2020)

MOXIE

MOXIE is a new technological device to be on board a Mars rover, with the purpose of demonstrating generation of oxygen gas by electrolytic decomposition of atmospheric carbon dioxide (Farley et al., 2020). MOXIE is only a ~1% scale model of an oxygen processing plant that can support a future manned mission to Mars by producing enough oxygen for a CH_4/O_2 propulsion system, allowing for ascent from the Martian surface (Williford et al., 2020). On April 20, 2021, MOXIE successfully converted carbon dioxide into oxygen.

MEDA

The Mars Environmental Dynamics Analyzer (MEDA) consists of a series of meteorological sensors including, a wind sensor, a barometer, and a relative humidity sensor. Additionally, the instrument also measures atmospheric temperatures at ~0.5 m and ~1.5 m above the surface. The MEDA was selected to characterize the atmospheric dust size and morphology to better understand its effects on the operation of surface systems and human health. The MEDA also documents the context in which samples for the MSR have been collected (Rodriguez-Manfredi et al., 2021).

Ingenuity

Ingenuity is a 1.8 kg, 1.2 m diameter helicopter with twin rotors, that is on board Perseverance to validate aerodynamics, control, navigation, and operation concepts for flights in the Martian atmosphere (Balaram et al., 2021). While Ingenuity is only a technology demonstrator, future helicopters with masses up to ~30 kg can follow the successful completion of the technology demonstration. Such future designs would have the capability to not only fly many kilometers daily, but even carry small science payloads. All communication from Ingenuity to the ground goes through Perseverance via radio (Balaram et al., 2021).

3. Background and geological setting

Mars accreted and differentiated not long after the formation of the Solar System. The presence of excess ^{182}W and ^{142}Nd in the Martian achondritic meteorite, ALH84001, indicate that internal differentiation happened within 10 to 30 Myr after the formation of the Solar System 4.5 Gyr ago (Carr & Head, 2009). A more recent study of the NWA 7034 meteorite backs up the theory that internal differentiation was rapid (< 20 Myr after the formation of the Solar System), using the $^{176}Lu/^{176}Hf$ isotopic decay system on zircons in the meteorite (Bouvier et al., 2018). The geological history of Mars is divided into three periods, the Noachian (4.1 Ga – 3.7 Ga), the Hesperian (3.7 Ga – 3 Ga) and the Amazonian (3 Ga – Present day). Their ages and corresponding time periods on Earth are shown in Fig. 5. Most geological activity is confined to the Noachian and Hesperian, in particular the relatively frequent impacts. These hypervelocity impacts caused melting of the surrounding rocks in the conversion of kinetic to thermal energy. The molten rock acted as a heat source capable of sustaining a hydrothermal system (Pirajno, 2009).

The evidence of past liquid water on the surface of Mars are found in valley networks. Basin lakes, such as Jezero crater (Fig. 6), are fed by one or more inlet channels, resulting in delta formation from the lakeward end of the inlet channel. The presence of an outlet channel indicates the minimum lake level in order to flood these basins (Fassett & Head, 2008).

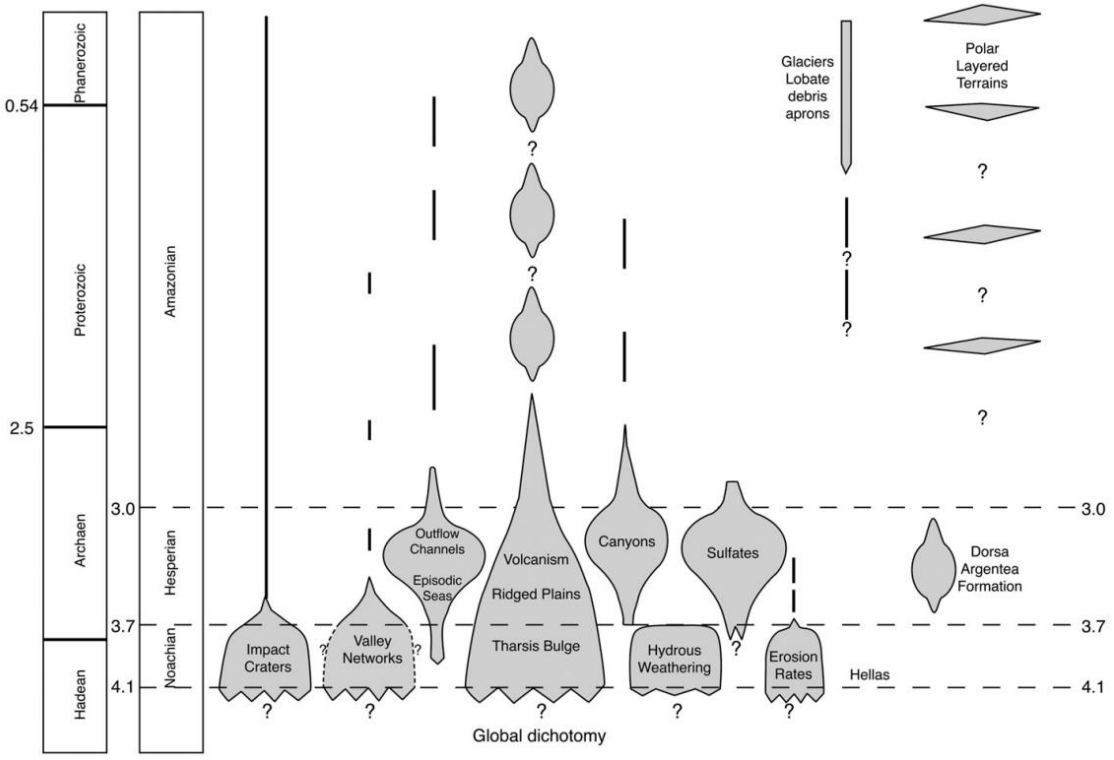

Fig. 5 - Geological activity and their relative importance as a function of time on Mars. The approximate boundaries of the major time periods of Mars are shown and are compared to similar major time subdivisions in Earth history. From: Carr & Head, 2009

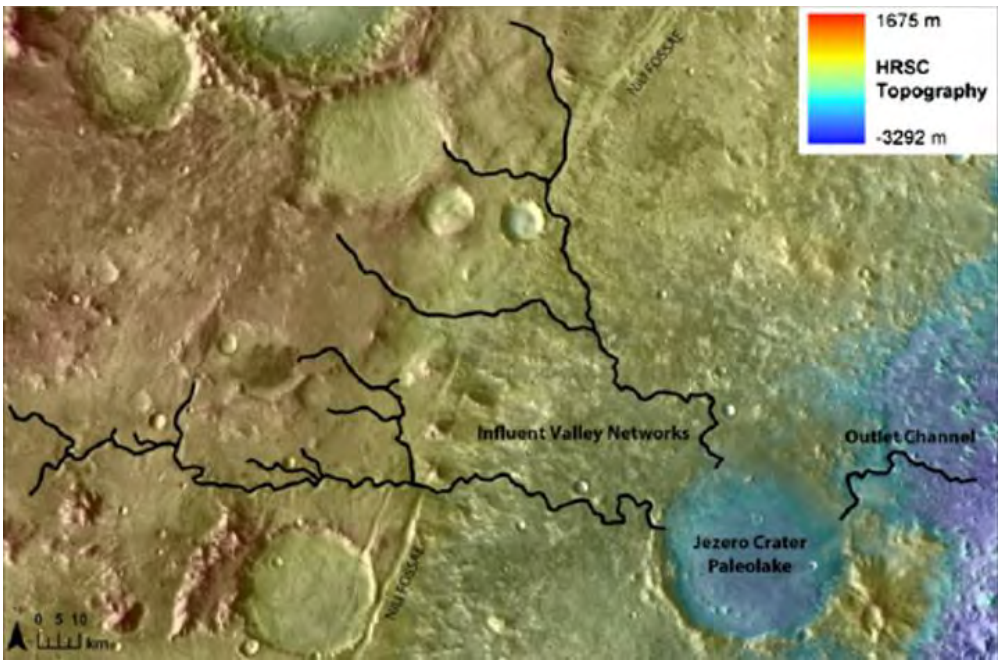

Fig. 6 – Jezero crater with valley networks highlighted. Inlet channels on the left and outlet channel on the right. From: Schon et al., 2012

The presence of liquid water on the surface of Mars in the Noachian and Hesperian, along with an intense magnetic dynamo and likely a denser atmosphere, contributed to an environment that was more habitable than at present. This potential ancient habitability of the planet has helped motivate an exploration strategy based on examining geological materials from this early period (Fassett & Head, 2011).

3.1 Regional geology

Jezero Crater is a ~45 km diameter impact crater located in the NW part of the Isidis basin, in the Nili Fossae region. The Isidis basin is a 1900 km diameter impact basin formed approximately 3.96-3.97 Gyr ago (Early-Mid Noachian) (Fassett & Head, 2011). Satellite measurements (See Section 4.1.3) of the Noachian basement unit of the region exhibits strong visible-near-infrared reflectance spectra of 0.9 μm and 1.8 μm consistent with low-Ca pyroxene, which suggests a lower-crust primitive igneous composition (Mustard et al., 2007). Additionally, the unit also exhibits narrow absorptions near 1.9 μm and 2.3 μm consistent with Fe/Mg-smectites, suggesting widespread alteration by groundwater or hydrothermal fluids. The Noachian basement unit is mantled by a regional olivine- and carbonate-bearing unit (Horgan et al., 2020). The Nili Fossae region is characterized by a series of approximately concentric graben, likely formed in response to the Isidis basin impact. The crustal material in the Nili Fossae region consists not only of units emplaced prior to the Isidis basin forming impact, but also of Isidis-related materials such as extensive brecciated units and ejecta. The Nili Fossae region is thought to be one of the locations on Mars, with the largest diversity and exposures of aqueous alteration minerals (Goudge et al., 2015).

The age of Jezero crater can be bracketed by the formation of the Isidis basin and the emplacement of a regional olivine-carbonate unit (3.82 ± 0.07 Ga; Goudge et al., 2015), which is inferred to be younger than Jezero crater as it overlaps the northern rim. The crater presently has a shallower depth profile than what is expected for a crater that size, which suggests substantial crater fill deposition. The crater fill is expected to be a combination of impact ejecta, volcanic deposits, lacustrine sediments, alluvial sediments, and aeolian deposits (Holm-Alwmark et al., 2021).

3.2 Geologic units of Jezero Crater

The geologic units of Jezero Crater can be divided into two groups, bedrock units and surficial units (Fig. 7). The naming scheme of the units is defined by Stack et al. (2020), who also describes the units in much greater detail and covers a more extensive area. The units presented in this thesis are not a complete representation of stratigraphic units present in Jezero Crater. The surficial units consist of aeolian bedforms, an undifferentiated smooth unit interpreted to mantle underlying bedrock, and talus cones from topographically elevated remnants and delta front (Stack et al., 2020). The bedrock units presented in this thesis are Crater floor fractured 1 (Cf-f-1), Crater floor fractured 2 (Cf-f-2), Crater floor fractured rough (Cf-fr), and deltaic deposits (here treated as one unit, although they can be further subdivided) (Fig. 7).

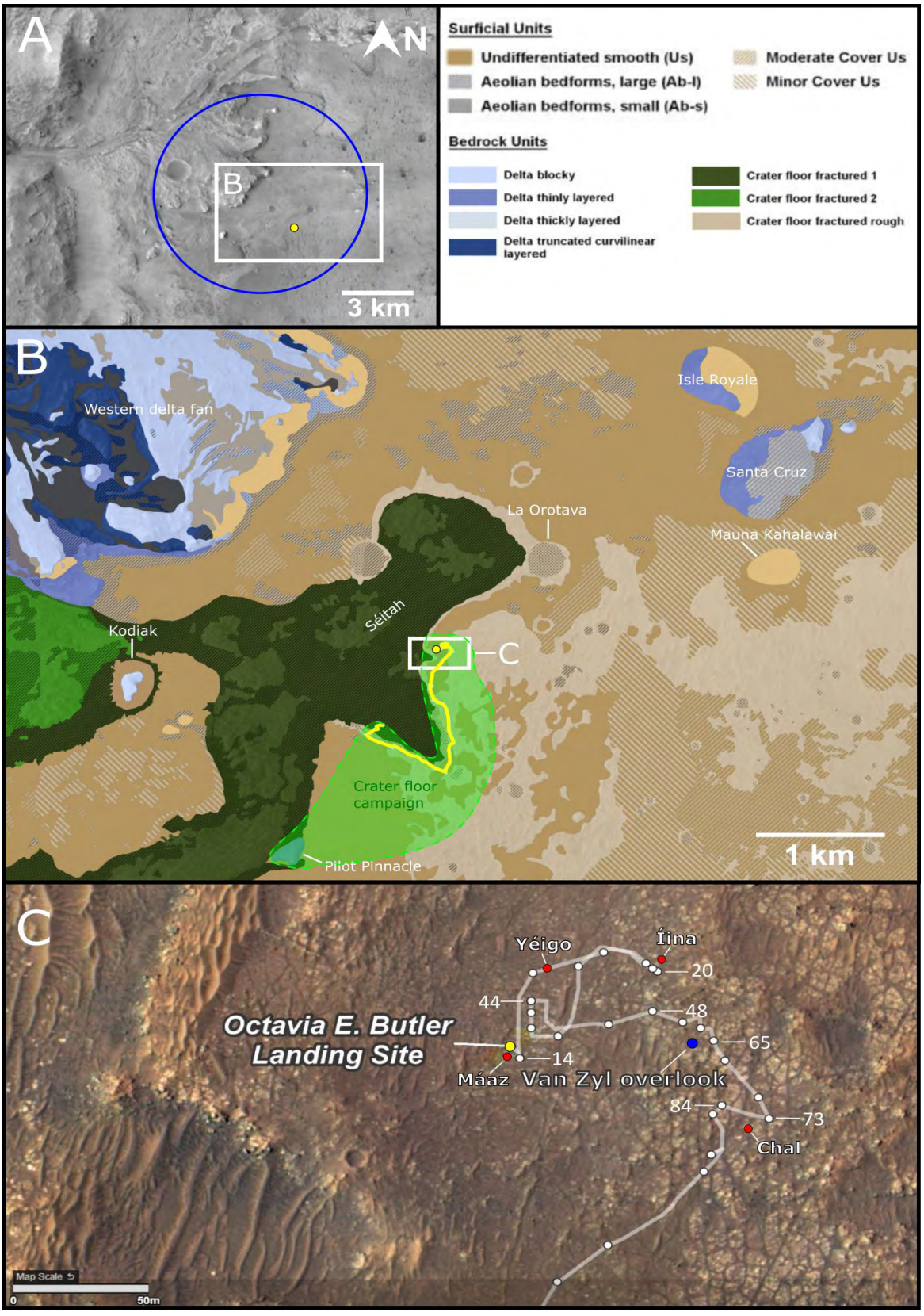

Fig. 7 – A) Location of the landing ellipse (blue ellipse) and landing site (yellow dot). B) Geologic map from the web-based GIS tool, CAMP, of the study site. The crater floor campaign is highlighted in green, the landing site is marked with a yellow dot and rover traverse with a yellow line. C) Detailed map of the rover traverse from the first 84 sols of the mission. Yellow dot: landing site; Blue dot: Van Zyl overlook, Red dots: Mastcam-Z target locations.

3.2.1 Crater floor fractured 1 and 2

Cf-f-1 is a unit that exhibits a mottled tone by linear mixture of dark and intermediate-toned sediments filling the crevices in a light-toned, blocky and fractured bedrock. It is primarily exposed below the -2530 m elevation contour, in two elongated areas near the northern and southern parts of the western delta front (Fig. 7) (Stack et al., 2020).

Cf-f-2 appears to be relatively similar to Cf-f-1, while Cf-f-2 is characterized by a rougher surface texture as a result of small meter-scale bumps and ridges, as well as being topographically higher than Cf-f-1 (Stack et al., 2020). Mineralogically, Cf-f-1 and Cf-f-2 also appear relatively similar and exhibit carbonate and olivine signatures in CRISM data (Horgan et al., 2020). Spectrally, the Cf-f units look very similar to the regional olivine- and carbonate-bearing unit in the Jezero area (Horgan et al., 2020). Horgan et al. (2020) suggests two scenarios for the origin of the units. Either they are local exposures of the regional unit, or they represent reworked aeolian or fluvial deposits sourced from the regional unit.

3.2.2 Crater floor fractured rough

The Cf-fr unit (Fig. 7) is a light- to medium toned, crater-retaining, fractured unit. The unit contains fractures at two distinct scales: small meter-scale fractures forming polygons, and large-scale fractures up to several hundred meters across (Stack et al., 2020). The unit comprises most of the Jezero crater floor, withs the western part of the crater floor mostly being covered by the undifferentiated smooth unit described below. This mantling by the undifferentiated smooth unit leads to less fractures, craters and rough textures to be observed. The unit is interpreted as lithified bedrock, in contrast to the overlying undifferentiated smooth unit which is interpreted as unconsolidated surface deposits (Stack et al., 2020).

3.2.3 Undifferentiated smooth

The Us unit (Fig. 7) on the crater floor is characterized by a medium to dark uniform tone and a general lack of any resolvable textures in orbital data. The unit is observed to overlie exposed bedrock units on the Jezero crater floor, within and on the delta, on deposits exposed along the inner margin of Jezero crater, and on the crater rim. Exposures vary in size, but the largest expanses are observed on the crater floor and the crater rim (Stack et al., 2020). The thickness of

Us on the crater floor is variable but is inferred to be thicker near the delta front. This variable thickness results in variable muting of underlying features, such as craters and fractures.

Spectrally the Us unit exhibits High-Calcium Pyroxenes (HCP) signatures, which are rare on the delta and absent in the Cf-f units. This HCP-bearing composition distinct from the other units in the crater, suggests a source consistent with more evolved magma compositions often associated with Hesperian and Amazonian volcanism (Horgan et al., 2020).

3.2.4 Delta deposits

The delta deposits in Jezero crater are constrained to two areas, the western and northern delta fans (Fig. 7), with the western delta fan being the most prominent and relevant to the Mars 2020 Mission. The western delta has been interpreted as a river delta that built out into a lake, from an inlet channel in the western rim of Jezero crater. The delta fan displays evidence of meandering distributaries that indicate that the deposits are of fluvial-deltaic origin, and contrasts features of alluvial fans as well as sediments deposited under unstable lacustrine conditions (Schon et al., 2012). The eastern edge of the western delta fan forms a distinct erosional scarp that exposes the internal layering of the delta. Further lakeward there are also multiple isolated topographical features, some of which are likely to be remnants of a past, more extensive western delta fan (Schon et al., 2012). An alternative hypothesis to the origin of some of the topographical features, is that they are of lacustrine origin rather than actual delta remnants, and as such referring to them as “delta remnants” could be misleading. As such, they will be referred to as “delta-associated remnant deposits” in this thesis.

4. Data used

The data used in this thesis can be divided into two parts. The orbital data phase prior to the launch of the M2020 mission, and the following in-flight phase.

The data used in this thesis primarily consists of in-flight data from the Mastcam-Z camera but orbital data, which was the basis of my bachelor’s project, has also been further processed for this thesis, and is published in Holm-Alwmark et al., 2021.

4.1 Orbital data

Data from before the landing of the Perseverance rover in Jezero Crater is limited to orbital data, from instruments aboard the various satellites orbiting Mars. The orbital data used in this thesis, is limited to instruments aboard the Mars Reconnaissance Orbiter (MRO), which entered orbit in March 2006 (Zurek and Smrekar, 2007).

4.1.1 HiRISE

The High Resolution Imaging Science Experiment (HiRISE) is a camera that provides detailed images (0.25 to 1.3 m/pixel) within the visible spectrum of 400-700 nm wavelengths of the Martian surface (McEwen et al., 2007). The purpose of the HiRISE camera is to document a broad range of geomorphologic features related to cratering, volcanology, tectonism, fluvial activity and more, particularly those in past and future landing sites.

By pairing up images of the same area, taken at different angles (stereopairing), it is possible to create a 3D Digital Elevation Model (DEM). The absolute accuracy of the DEMs is limited by the ability to tie the stereomodels to ground control. The vertical precision of the DEMs is approximately ~25 cm in 1 m^2 areas, and depends on the convergence angle of the stereopair, the image resolution and the matching error (McEwen et al., 2007).
The HiRISE images and stereo derived DEMs used in this thesis were acquired from the web-based GIS tool CAMP and the source files are available on GitHub[1].

[1] https://github.com/NASA-AMMOS/MMGIS

4.1.2 CTX

The Context Camera (CTX) is designed to provide context images for data acquired by other MRO instruments, as well as observing features of interest to NASA's Mars Exploration Program in the search for candidate landing sites. The spatial resolution from MRO's orbit is ~6 m/pixel (Malin et al., 2007). The objectives of the CTX camera are to document the geology and geomorphology of layered outcrops, fluvial landforms, aeolian landforms, volcanic features, and impact craters on a global scale (Malin et al., 2007). The low resolution of CTX compared to HiRISE does in turn mean that the coverage of Mars is much greater. In 2017 the CTX coverage of Mars surpassed 99% (NASA MRO, 2017).

The CTX mosaic used in this thesis was acquired from the Mars 2020 Science Team Wiki site.

4.1.3 CRISM

The Compact Reconnaissance Imaging Spectrometer for Mars (CRISM) is a hyperspectral camera on the MRO operating in the 362-3920 nm spectral range (i.e., observing mainly reflected sunlight). CRISM acquires global data at a subset of 72 wavelengths sufficient to characterize mineralogy at a resolution of 100-200 m/pixel. In regions of interest CRISM can acquire images at full spatial and spectral resolution at 15-19 m/pixel at a subset of 545 wavelengths, providing high sensitivity to detect low abundances of key minerals, such as phyllosilicates, iron and carbonates (Murchie et al., 2007).

4.2 Mastcam-Z on the Perseverance rover

Data from Mastcam-Z is used to provide detailed documentation of morphology, topography, and geologic context along the traverse of the Perseverance rover through multispectral, stereo, and panoramic images (Bell et al., 2021). The images provided by Mastcam-Z are used to constrain the mineralogic and physical properties through detailed rock/regolith analysis.

Prior to analysis all images must be reflectance calibrated, as the illumination conditions are highly variable. For this reason, the calibration targets are frequently imaged, particularly in conjunction with multispectral observations. First the raw images are converted through a series of steps (Fig. 8)(including reduction of noise from within the cameras and the DEA) into

radiance calibrated images (Hayes et al., 2021), which in turn are converted to reflectance (I/F) calibrated images (Kinch et al., 2020).

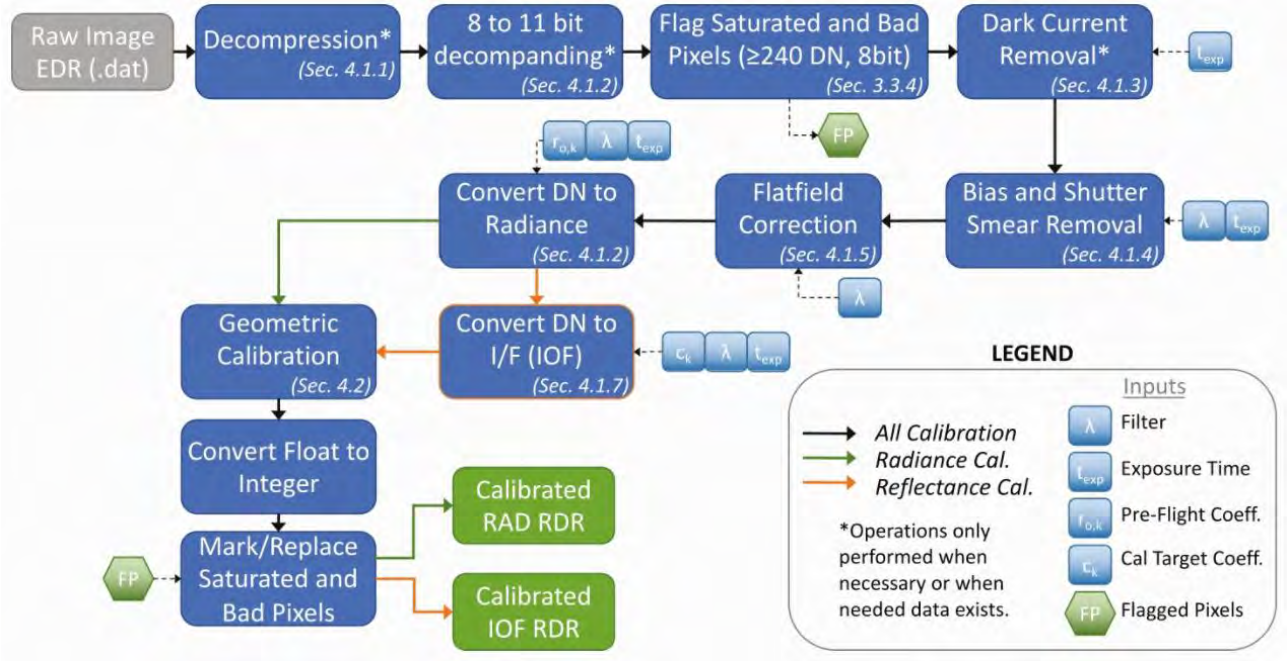

Fig. 8 – Flowchart outlining the steps in the Mastcam-Z radiometric calibration pipeline. The sections referred to can be found in: Hayes et al., 2021

The I/F calibrated images are then used to create a series of spectral parameter products, to help scientists identify spectral variations more easily. From the acquired multispectral observations it is possible to extract spectra from regions of interest within the I/F calibrated images, allowing for correlation between the physical properties of the rocks/regoliths, and their VNIR (Visible and Near-Infrared) spectral properties. The spectra extracted from Mastcam-Z images are of low spectral resolution but high spatial resolution. The spectral properties can then be compared to lab spectra (Fig. 9), for interpretation. For observations on a larger scale than what fits in a single frame, Mastcam-Z can also produce RGB and multispectral panoramas and mosaics through a series of images.

The DEA instrument flight software (iFSW) receives commands generated by the science and engineering teams on Earth, executes commands and transmits the results back to Earth. In the process, the iFSW also implements auto-focus, auto-exposure and “Z-stack” algorithms for image acquisition. Z-stacking is a process that combines multiple frames at various focus settings to create one best-focus frame (Bell et al., 2021).

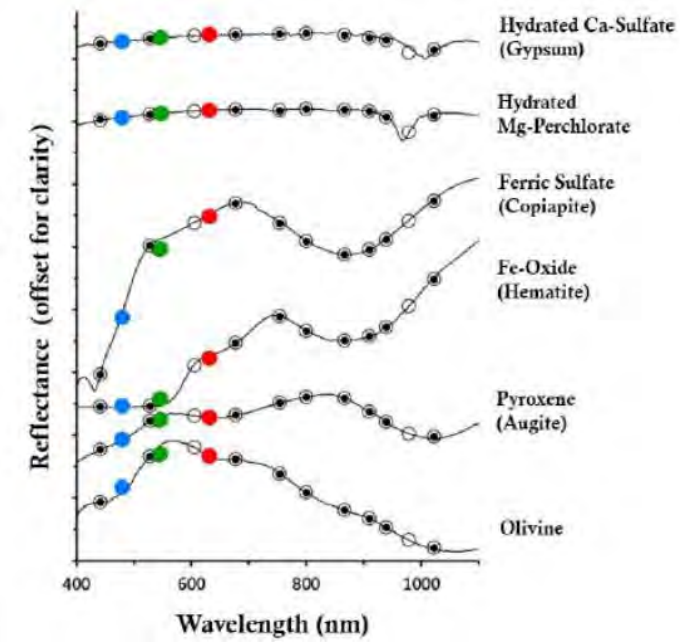

Fig. 9 – Lab spectra of Mars-relevant hydrated minerals, ferric sulfate, iron oxide, and ferrous silicates convolved to the Mastcam-Z narrowband (open circles) and RGB filters (colored circles). Black circles are filters heritage from MSL/Mastcam. From: Bell et al., 2021

All Mastcam-Z products used in this thesis were acquired from internal Mastcam-Z databases, but radiance and reflectance calibrated data from the first 180 sols is publicly available on NASA's planetary data website[2], although they might be marginally different due to evolving calibration processes.

[2] https://pds-imaging.jpl.nasa.gov/data/mars2020/mars2020_mastcamz/

4.2.1 Mastcam-Z file naming scheme

A lot of information about each Mastcam-Z image is encoded in the 58-character names. Table 2 shows how each segment of characters is decoded.

Single Image Raw Mastcam-Z 58-character file naming scheme	
Example:	
ZRF 0003 0667220795 000FDR N0010052AUT 04096 034085J01.png	
Character	**Description**
ZR	Two-digit Instrument Identifier:
	"ZL"=Mastcam-Z left,
	"ZR"=Mastcam-Z Right
F	One-digit Filter number:
	Values = 0-7 or "F", where "F" also = filter 0
0003	Four-digit Primary Timestamp: mission Sol number
0667220795	Ten-digit Secondary Timestamp:
	Spacecraft Clock Time or SCLK (mission time)
000	Three-digit Tertiary timestamp: SCLK milliseconds
FDR	Three-digit Product Type identifier
	FDR = "Final Data Record" produced by JPL for raw images
	others include EDR, ECM, EBY, EJP, EVD, ERD
	details to be provided in NASA/PDS data release documentation
N	One-character "thumbnail or not?" flag :
	"T"=Thumbnail, "N"=Non-Thumbnail (normal image)
001	Three-digit Site location count where the data were acquired
	Science team will update the site counter as we traverse
0052	Four-digit Drive count position within a site location
AUT_04096	Nine-digit Sequence id: Instrument (4) then Sequence ID (5)
	"AUT " is an alternate designator for sol 1-4 cruise software
	"ZCAM" is the typical instrument designator
034	Three-digit focal length indicator, in mm
0	One-digit downsampling flag:
	0 means 2^0 downsampling = full resolution.
	1 means 2^1 downsampling which uses 2x2 summing, etc.
85	Two-digit JPEG compression quality flag
	00 = JPEG lossy compressed thumbnail
	01-99 = JPEG lossy compressed quality level
	LU = Losslessly uncompressed)
J	One-digit Producer of product ("J" = JPL, "A" = ASU)
01	Two-digit Product Version number
png	Three-digit file type extension (PNG, JPG, IMG)

Table 2 – Mastcam-Z 58-character naming scheme of a single image.

5. Methods

Just like the data collection, the methods used in this thesis can also be divided into the orbital data phase and M2020 in-flight phase. As mentioned, the orbital data processing resulted in a more refined and developed product based on my bachelor's project. This work contributed to the paper by Holm-Alwmark et al., 2021, on constraining the stratigraphic relations and temporal ordering of deltaic and other crater floor deposits in Jezero crater. The in-flight methods consist mostly of processing of my own work during my time as a student collaborator on the Mastcam-Z science downlink team, though some products by team colleagues are also included.

5.1 Orbital data

5.1.1 Topographic profiles

The presented topographic profiles are based on the HiRISE images and derived DEMs extracted from CAMP, and further processed in the open-source GIS software, QGIS. The locations of the profiles were carefully selected to include points of interest, such as unit boundaries, delta remnants, and delta-associated remnant deposits. The profile lines are plotted on an elevation contour map of the western delta, which was created in QGIS. The profiles are ranging from 4500-8000 m horizontally, with an elevation variation of approximately ~180 m at the extremes. The data points for the profiles were extracted into .csv-files at ~1 m resolution, using the QGIS "Terrain Profile"-plugin. A MATLAB script was set up for efficiently creating visual representation of the .csv-files and manipulating an axial ratio of 1 (Making sure the axes are the same scale is important when analyzing topographic features). The profiles were also created in vertically exaggerated versions allowing for easier identification of topographic features. Two profiles also had their X-axis shortened, to further enhance topographic features. Finally, the raw MATLAB figures were polished and colored in the open-source vector graphics editor, Inkscape.

5.2 In-flight data

When Perseverance landed on Mars on February 18th, 2021 (Fig. 7A), the Mars 2020 mission transitioned from its cruise phase to surface transition. This phase is critically important to assess first time events of the rover, such as communications processes, payload functions, deployment of the arm, and transitioning the rover software from cruise phase to surface phase. Naturally these early phases do not leave much room for scientific observations, and thus was a relatively quiet phase scientifically. The surface transition phases are followed by science campaigns, where scientific observations are the primary objectives. The first science campaign is known as the "crater floor campaign", during which Perseverance will explore the crater floor, investigating and sampling the deepest identified geologic units within Jezero crater.

5.2.1 Participation in the Mastcam-Z downlink team

The team operating Mastcam-Z can be subdivided into two teams: uplink and downlink. The two teams work together daily in the daily planning cycle. The uplink team sends commands to the rover, to be executed the following sol. The downlink team handles products returned to Earth and generates second-order data products, that may act as input for decisions to be made for that same sol or for planning further ahead. The downlink team typically consists of 2-3 Payload Downlink Leads (PDL-n) that are responsible for generating reports of accounted data, instrument health, and image statistics. Additionally, the downlink team also consists of a science PDL (sPDL-1), responsible for generating second-order data products based on incoming data and reporting to the broader Mastcam-Z and M2020 teams. My participation in the Mastcam-Z science downlink team started as science Payload Downlink Lead (sPDL) on the support team. The support team was commissioned to assist the sPDL-1 in documentation and production second-order data products for scientific analysis. This support team allowed for operationally less-experienced people, such as myself, to participate in the Mars 2020 mission and not only learn from the experience, but also contribute with meaningful support to the sPDL-1. The support team consists of three roles: Support Team Lead, Documentarian and Data Analysts, each responsible for specific tasks. The Lead is responsible for facilitating work to be done by the rest of the support team, as well as provide assistance if required. The Lead is also responsible for communication between the support team and other Mastcam-Z teams on both

uplink and downlink sides. The Documentarian is responsible for generating a scientific report of the downlink events of the sol, including a summary of the observational data received, data products made by the team, and notable discoveries in the images. The Data Analysts are responsible for producing second-order data products to be passed on to the sPDL-1, for potential inclusion in the PDL report and/or presentation to the broader Mars 2020 team. Most internal Mastcam-Z operational communication is carried out through chat (Mattermost) or video communication (Zoom).

During the first 10 weeks of operations, everything was scheduled according to Mars time, which due to the longer diurnal cycle of Mars, meant that shifts were starting round the clock. A typical shift would start with getting oriented, by checking the PDL report, support documentarian report, and Mattermost chat history from the previous sol, as well as looking at the reported activities planned by the uplink team. Following is a tag-up meeting with the purpose of connecting with the rest of the support team and PDLs, to briefly run through the expected downlink products, coordinate second-order data product generation, and catch up on any leftover tasks from the previous sol. Shortly after, immediately prior to the uplink team starting their shift, the uplink and downlink teams have a tag-up meeting to brief each other about activities relevant to the shift. After the first 10 weeks, operations shifted to Earth time to allow for people to work at more normal work hours – at least those located geographically near the eastern Pacific. This in turn leads to a desynchronization between shift times and rover operations, resulting in days without operational efforts. On alternating nominal days there are M2020 team wide Science Discussions (SD) and Campaign Implementation (CI) discussions. The purpose of these meetings is for the various teams to present and discuss the most recent observations, as well as the upcoming rover plans. The exact end of a shift is flexible and is highly dependent on the amount and time of downlinked data, planned meetings, and discussions. Once the second-order data products are made, meetings are over and discussions coming to an end, the sPDL releases the support team.

My participation in the Mastcam-Z science downlink team consisted of 27 6-8 hour shifts between sol 13 (March 1, 2021) and 82 (May 10, 2021), which towards the end also included shifts as sPDL-1.

5.2.2 Multispectral parameter products

Almost all second-order data products are made in a set of Interactive Data Language (IDL) tools, originally developed for the MER mission (Section 2.2), called MERtools. MERtools has since then been further developed and acts as validated tools for the MSL and M2020 missions as well. MERtools consists of a range of tools, including MERstamps, MERview, MERspect, and MERmap.

MERstamps (Fig. 10) is a tool that allows for a quick overview of downlinked data. It is primarily used as identification of incomplete frames, and as an entry-point for further processing. From MERstamps you can continue to MERview or MERspect with a selection of images of your choice.

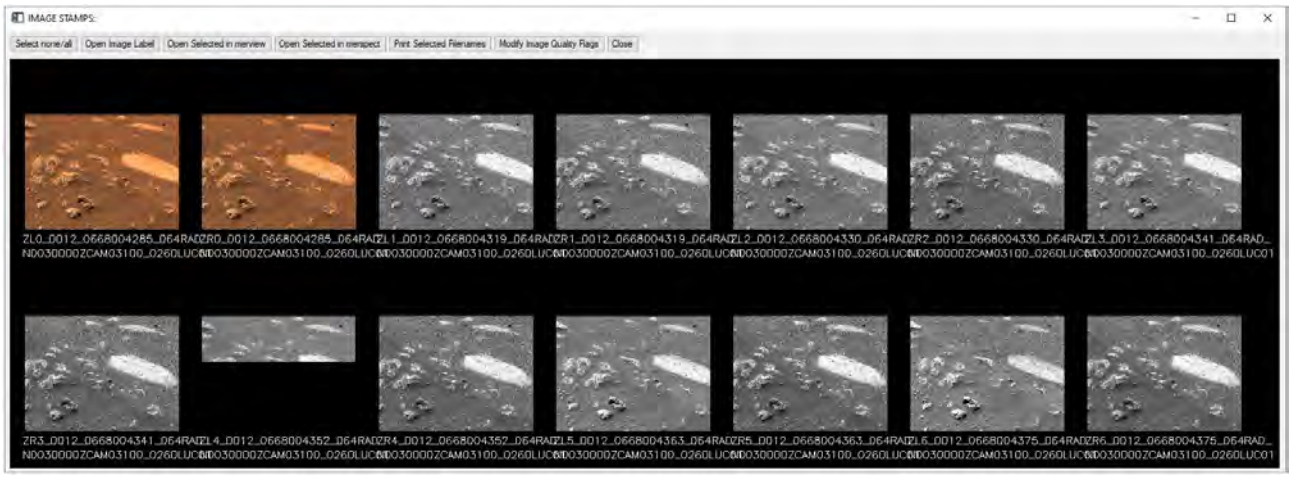

Fig. 10 – MERstamps interface with a multispectral dataset from sol 12 (Máaz target). In this example filter 4 on the left eye (ZL4) is incomplete, due to a lack of transmitted data packages.

MERview (Fig. 11) is a tool that allows for a detailed look of the frames and their properties, as well as manipulation of color channels (RGB) and their stretch. It is used both for viewing single frames as well as mosaics (described later in this section) and writing images at various formats and resolutions.

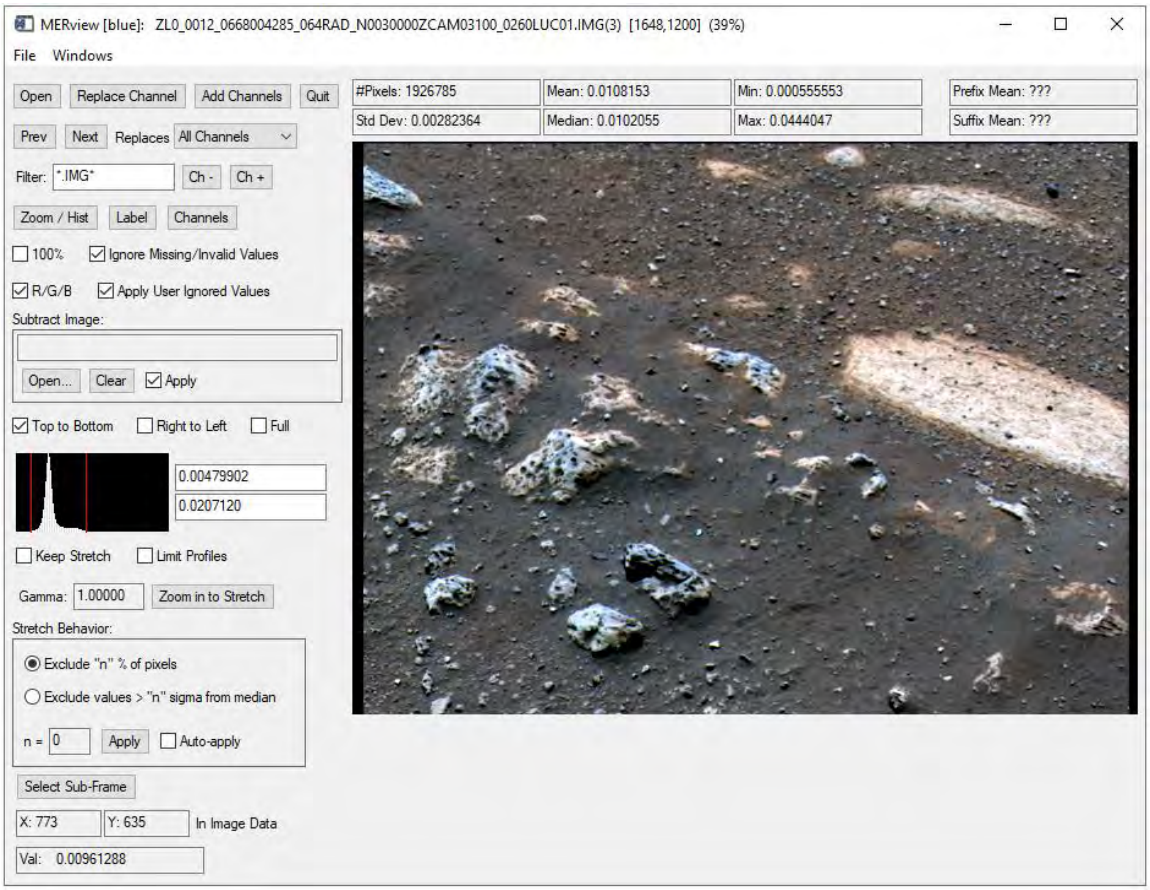

Fig. 11 –MERview interface with an example of a manipulated RGB image of Máaz target with stretched colors.

MERspect (Fig. 12) is a highly diverse tool, that is used for the generation of second-order multispectral data products. It uses the narrowband filters (L1/R1-L6/R6) to create decorrelation stretches (DCS), band depth maps, as well as slope maps. In a DCS the color differences in a multispectral dataset are maximized, to bring out features that would otherwise be difficult to distinguish. A band depth map is generated by using three filters of different wavelengths. The band depth is calculated by a ratio between the reflectance of the band center, and the reflectance of the continuum at the same wavelength as the band center. The continuum is a straight line defined by the two “shoulder” filters on either side of the center. Slope maps are generated by calculating the difference of reflectance values divided by the difference in wavelengths. As such, each pixel represents a value based on the ratio between two wavelengths. Additionally, MERspect can also be used to select certain regions of interest within the frames and extract the spectral properties of those specific regions. These multispectral products are used in further scientific investigation and allows for observations that might not be visible in natural color images.

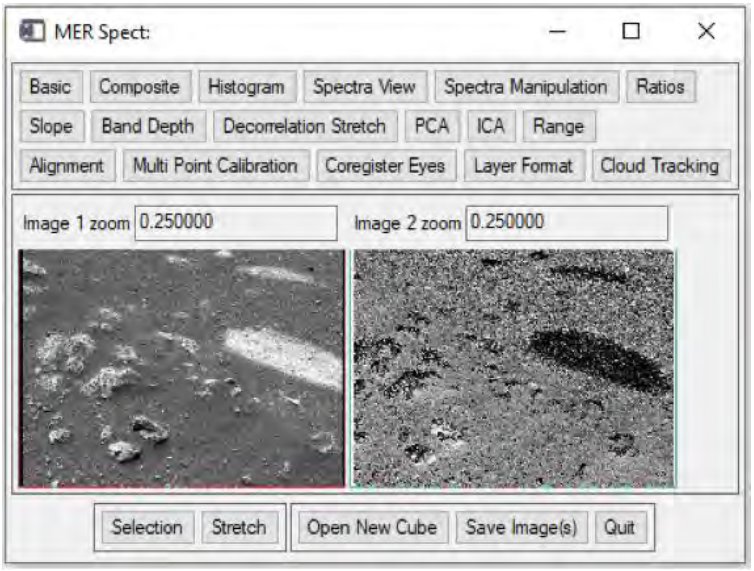

Fig. 12 – Main frame interface of MERspect showing the diversity of tools within. In this example the right frame is displaying a slope map in the infrared spectrum (801-1012 nm).

5.2.3 Mosaics and panoramas

When a target is too large or the focal length is too high to fit the target in one frame, the planned activity will include a series of frames (Fig. 13). For scientific purposes it is often desirable to make observations at high focal lengths for the best possible resolution, despite the field-of-view being reduced. Panoramic images are also taken as the rover traverses, as they allow for observing large areas in the search for potential targets of interest.

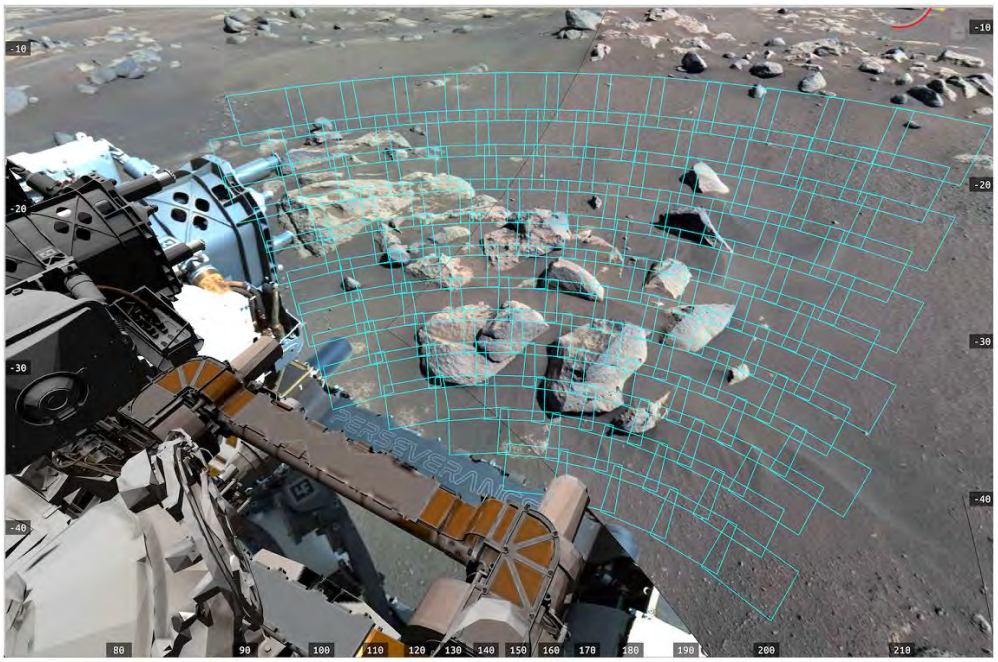

Fig. 13 – Footprint image of the planned mosaic seq. 08100 of the Van Zyl workspace from sol 53

The geometric data elements are stored within the frames, allowing for a tool such as MERmap (Fig. 14) to stitch the images together to form a mosaic. The production of mosaics is not trivial and requires a tool such as MERmap, as a three-dimensional spherical signal must be projected onto a two-dimensional medium. In the process of making a mosaic look smooth (i.e.,, invisible seams between frames), the images must be cropped free of inactive pixels and flatfield corrected. Though sometimes mosaics are created from raw images, in order to speed up the second-order product generation process. Inactive pixels are framing the actual image and are areas in the CCD (Charge-coupled Device) that are not exposed to light, but still receives signal. They are as such used to estimate the effects of signal unrelated to light. This correction is designed to minimize pixel-to-pixel variations in an image as well as optical variations across the mosaic. The flatfield correction is designed as a multiplicative correction that brings every pixel to the same average response. Flatfield correction is discussed in much greater detail in Hayes et al., 2021.

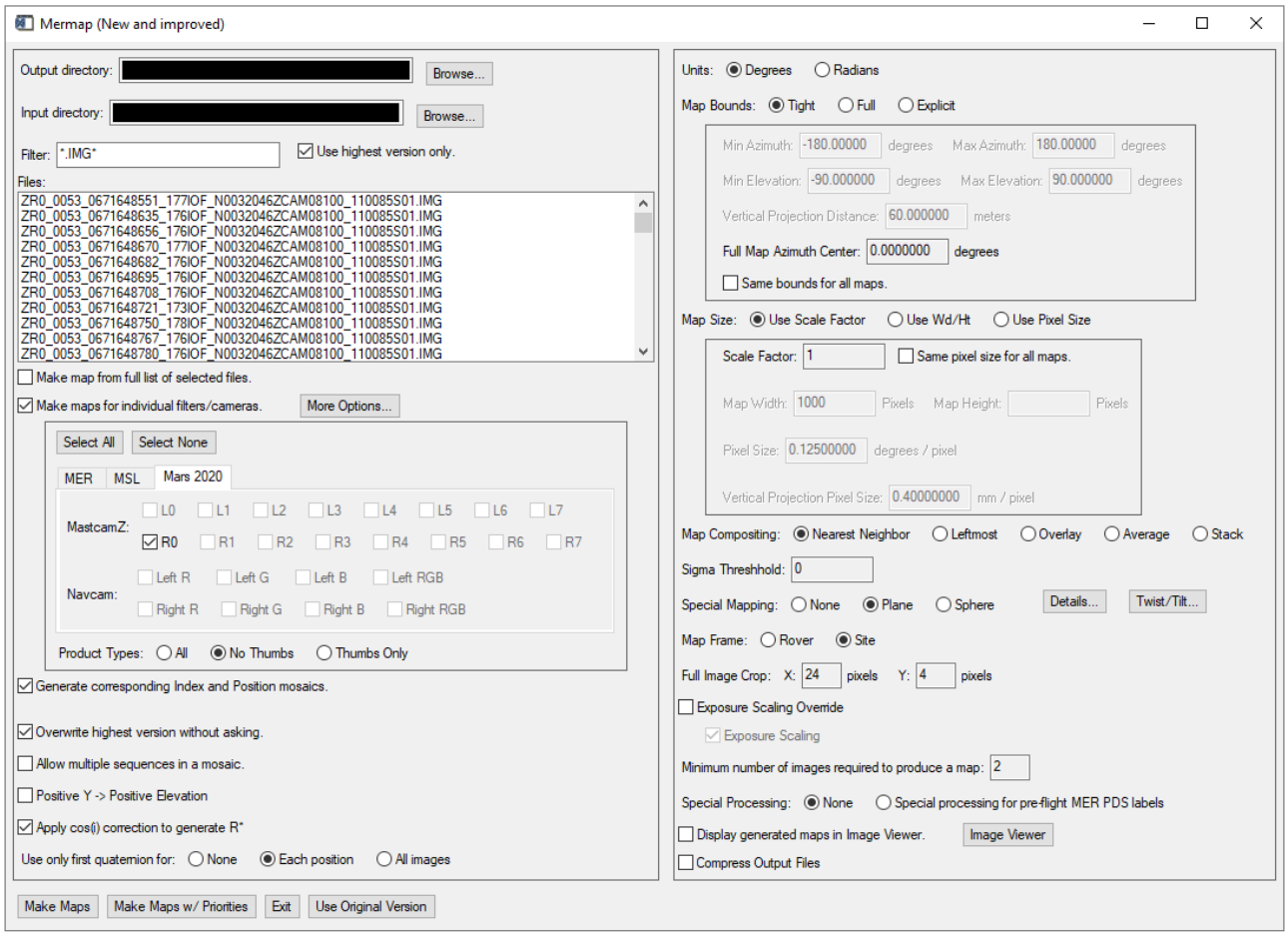

Fig. 14 – MERmap interface in the process of making a mosaic.

5.2.4 Automated product generation

Since my participation in the Mastcam-Z science support team, many of the manual product generation processes have been integrated in the pipeline. The automated processes are based on the preceding manual work by the Mastcam-Z downlink science and science support teams. Most of the results presented in this thesis are automatically generated second-order data products which are essentially identical to the products manually generated. One set of manual data products are included for reference.

6. Results

The presented results include work made in the pre-flight phase prior to landing (6.1), and the in-flight phase after landing (6.2). The orbital results include a topographic map and profiles based on orbital data. The in-flight results include Bayer pattern RGB images, multispectral images, mosaics, and mineralogic interpretation based on spectra from the Mastcam-Z camera on the Mars 2020 Perseverance rover.

6.1 Orbital data

6.1.1 Topographic profiles

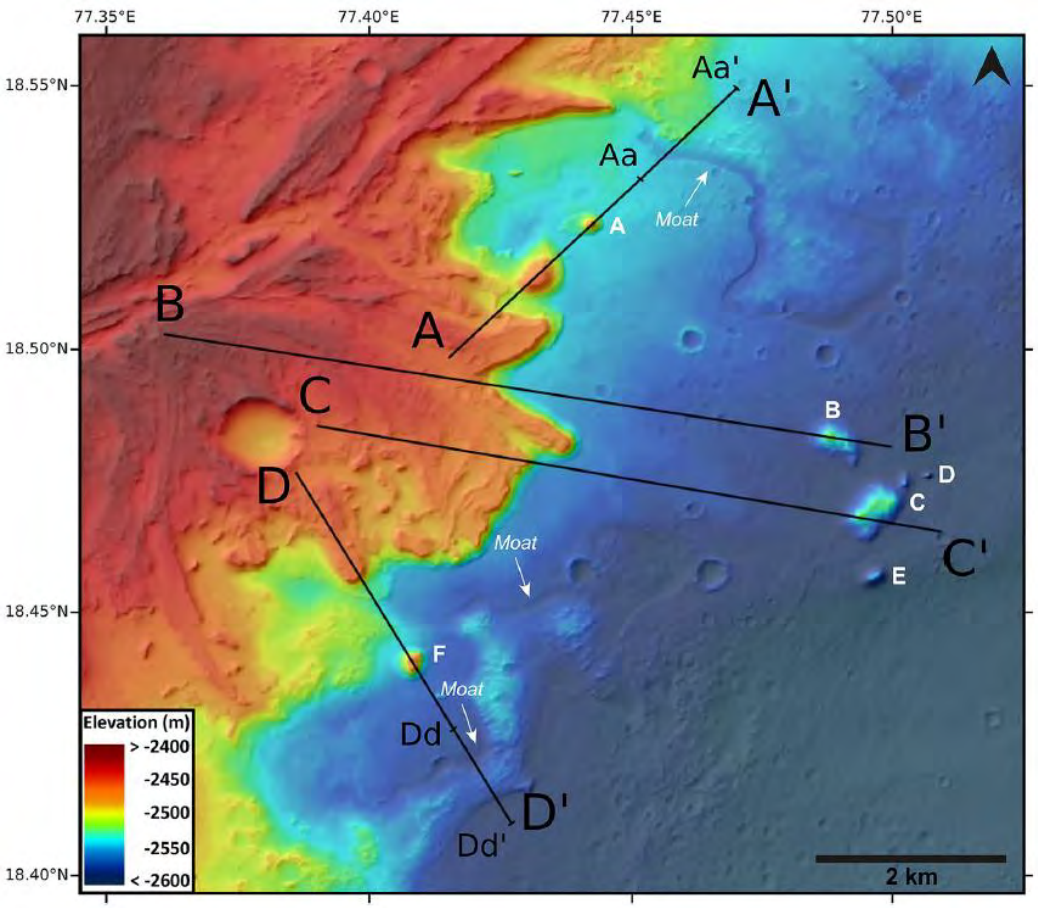

Fig. 15 – Digital Elevation Model of the western part of Jezero crater, with the western delta fan on the left side of the image. Transects labelled A-A', B-B', C-C', and D-D' represent the location of topographic profiles shown in Fig. 16. Local topographic features labelled in white bold text (A-F) are delta-associated remnant deposits. White arrows point to local topographic depressions at unit boundaries (moats). Elevations are relative to the areoid of Mars. This figure by me is figure 6 in Holm-Alwmark et al., 2021.

Topographic profiles were one of my earliest investigations made for analyzing the stratigraphic relations of the units present in Jezero crater. The profiles presented in this thesis are based on a series of topographic profiles I worked on during my bachelor's project. For this thesis, I relocated, combined, and extended them in length, to include as many topographic features (such as moats and delta-associated remnant deposits) and unit boundaries as possible. The visual presentation of the profiles was refined to reach a standard for publication in Holm-Alwmark et al., 2021. Additionally, a topographic map was created to visualize the topographic variations in the study area and show the locations of the topographic profiles (Fig. 15).

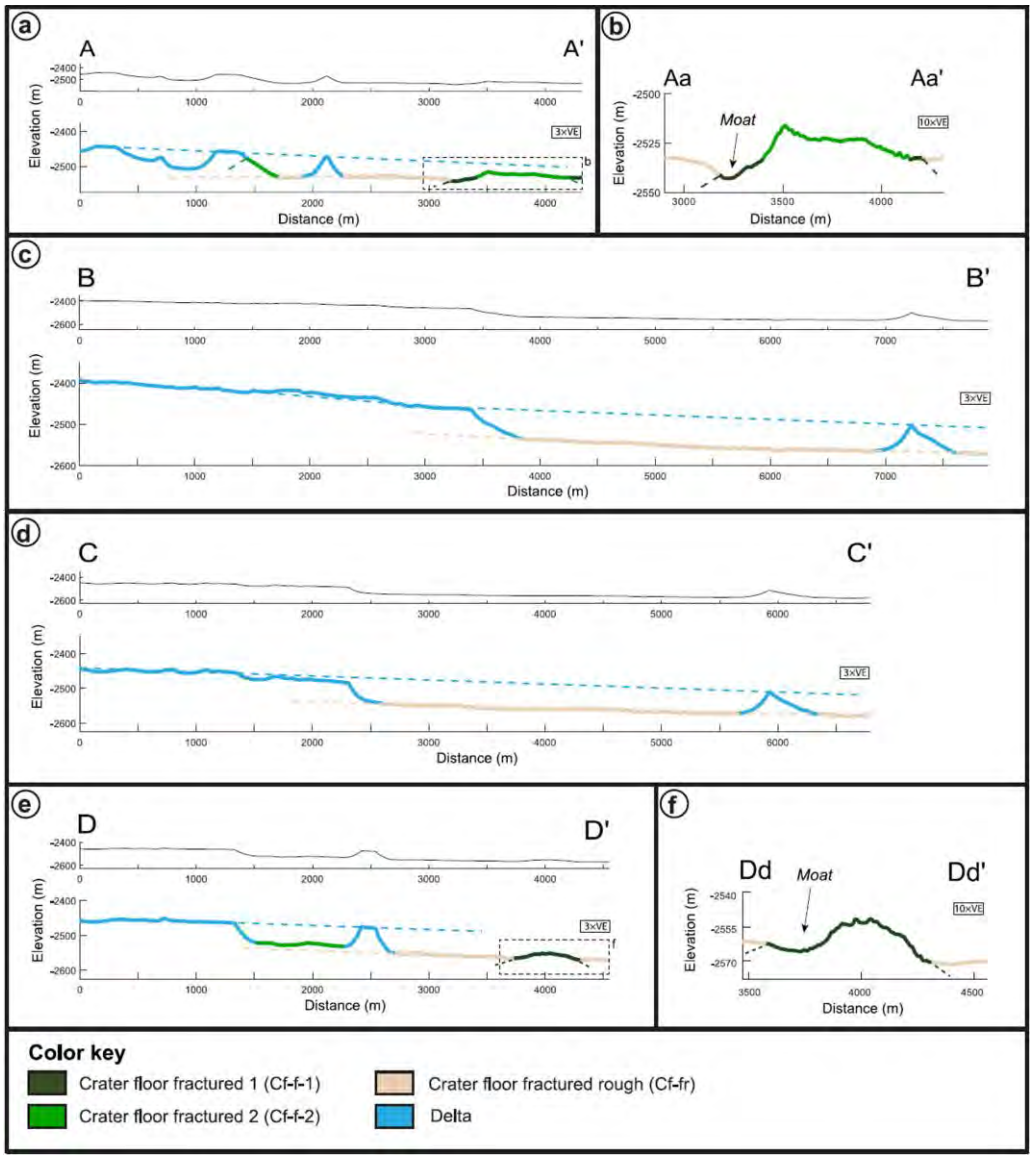

Fig. 16 – (a-f) Topographic profiles (locations in Fig. 15) extending from the western delta fan onto the crater floor. All profiles are made in two versions. One with x/y-ratios of 1, and one with 3 times vertical exaggeration (VE). Colored lines in the profiles represent the corresponding geologic units. The dashed blue lines represent possible past extensions of the western delta and the dashed beige lines represents the apparent slope of the crater floor (Cf-fr and overlying Us). Elevations are relative to the areoid of Mars. This figure by me is figure 7 in Holm-Alwmark et al., 2021.

The topographic profiles are presented in two versions (Fig. 16). One without vertical exaggeration representing the actual topographic variations, by making sure the x- and y-axis ratio is 1 (100 m on the x-axis is equal to 100 m on the y-axis). This processing is important when extrapolating the current extent of the delta and estimating the regional slope of the crater floor. From these profiles additional vertically exaggerated profiles were made, to visually enhance the topographic variations in the profiles. Lastly two detailed profiles (Fig. 16, b and f) were further vertically exaggerated to make the topographic boundary depressions (moats) stand out.

On each of the profiles a possible past extent of the western delta fan was plotted (dashed blue lines). The purpose of them, is to show that a possible past extent of the delta could have reached as far as the eastern delta-associated remnant deposits (Fig. 15, B-E). An important caveat to these extended delta lines, are that they were plotted by hand resulting in some uncertainty. The topographic profiles also show that the Cf-fr unit has a slope that appears to be equal to the upper surface of the western delta, except in profile A in which the delta portion of the transect cuts through a plateau and a channel. The inclination of the crater floor also appears to be along the axes that are radial to the delta in profiles B, C and D.

The elevation of the delta is generally 50-70 m higher than the crater floor, with the boundary between the two units being covered by a sediment cover, as a results of erosion of the delta. The steepness of the delta scarp varies between 6° (Profile B) and 27° (Profile C), although the sample size is very limited. The delta/Cf-fr-Us boundary does not appear to have a local topographic depression. Just like the delta scarps contact with Cf-fr-Us, the delta-associated remnant deposits also do not exhibit moats at their contacts with Cf-fr-Us. On the contrary, the contacts between Cf-f-1 and Cf-fr-Us displays distinct moats (Figs. 15; 16b; 16f), especially on the western side of the exposed Cf-f-1 unit. These moats can easily be observed in the topographic map (Fig. 15).

6.1.2 Mineralogy by CRISM

The mineralogy of the study area is available through a CRISM layer in CAMP, showing the mineral distribution of mafic minerals; Olivine, LCP, and HCP (Fig. 17). By comparing the CRISM map with the photogeologic map (Fig. 7), it is evident that the Cf-f-1 unit is characterized by a strong olivine signature, Cf-fr by HCP, the delta and delta-associated remnant

deposits by LCP, and the Us unit by LCP. The area proximal to the delta is characterized by HCP (Cf-fr) overlain by LCP (Us).

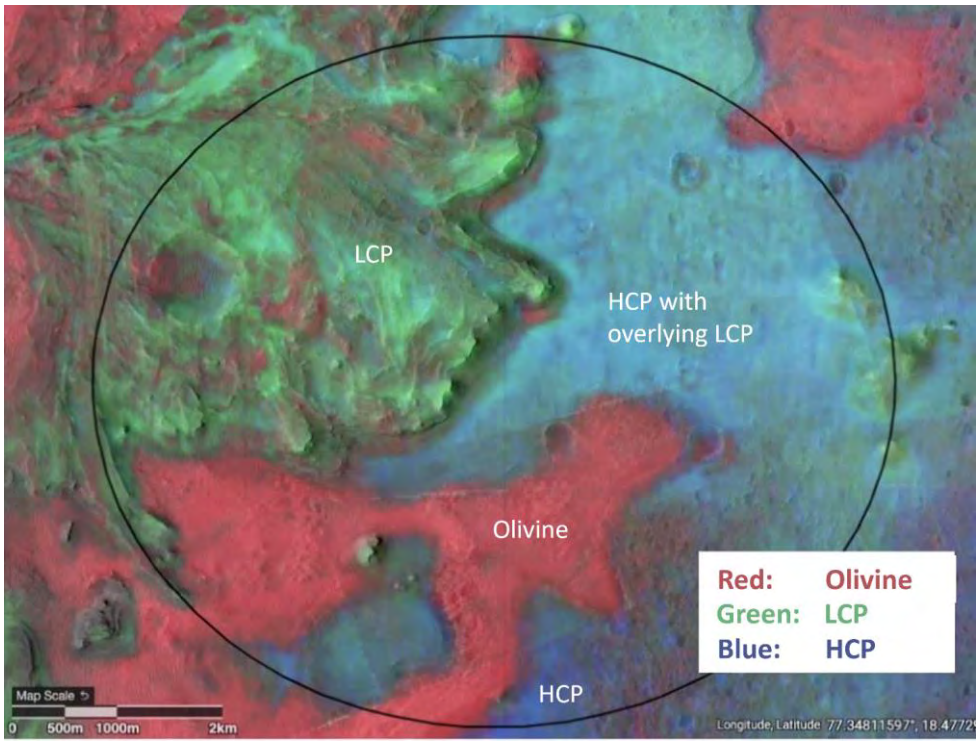

Fig. 17 – Distribution of mafic minerals near the western delta fan in Jezero crater, detected by the CRISM instrument aboard the MRO. Modified figure from: Horgan et al., 2020.

6.2 In-flight data

6.2.1 Rock classification

After landing a variety of rock morphotypes were observed. The morphotypes (Fig. 18A, 18B) are referred to as “pitted rocks”, “pavers” and “massives” in this thesis. The pitted rocks are characterized by ~1 cm scale pits and appear as both dark and light toned (Fig. 18A). The pavers are lighter toned, rubbly rocks that are mostly embedded within the regolith (Fig. 18B). The massive rocks have a lighter color at the base with darker tops and appear to have an abrupt transition from rough to smooth texture (Fig. 18B).

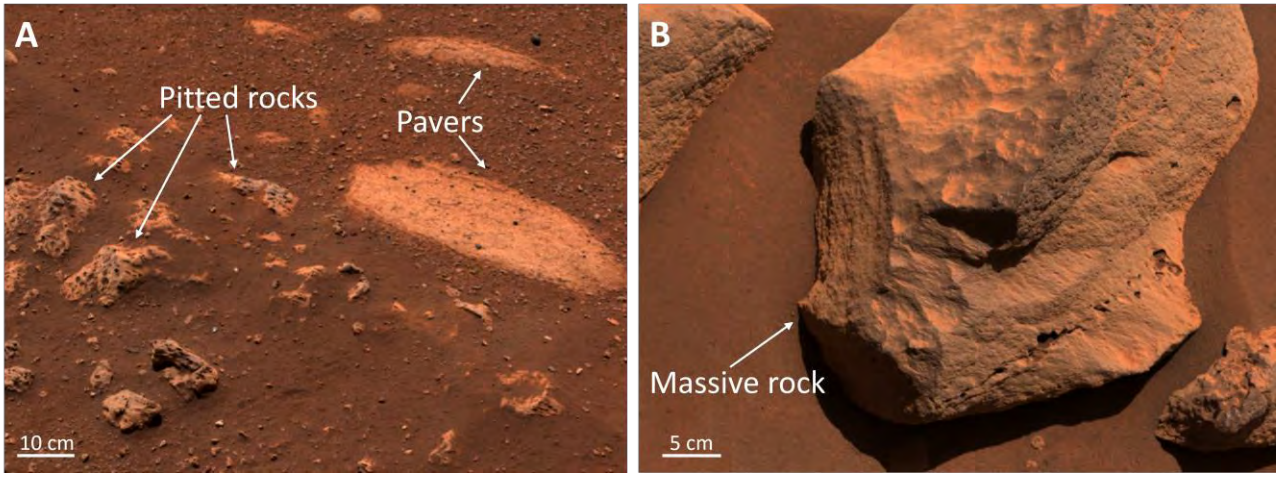

Fig. 18 – A) Pitted rocks and pavers in an estimated true color RGB image of Máaz target, sol 12, seq. 03100. B) Massive rock in an estimated true color RGB image of Bidziil target, sol 56, seq. 03115

Rock classification is based not only on their morphology but also spectral signatures. Fig. 19 shows examples of spectral signatures of Low-Calcium Pyroxenes (LCP) and olivines. The spectral signatures can look quite similar to Mastcam-Z, and as such we require additional information (e.g., SuperCam, SHERLOC, or PIXL) to confidently interpret the mineralogy of our targets.

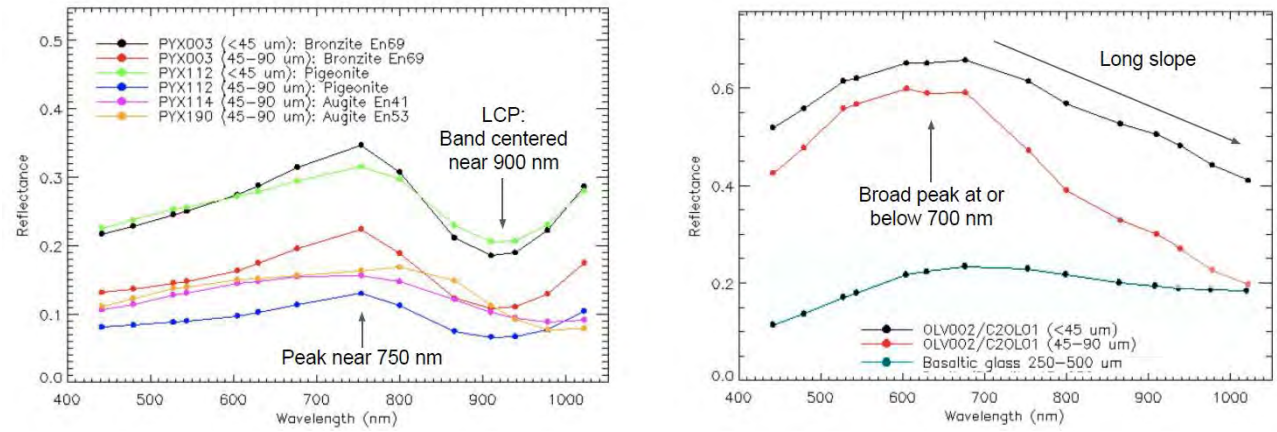

Fig. 19 – Spectral signatures of primary mafic minerals. Low-Calcium Pyroxenes (left) and olivines (right). From: Science Discussion sol 48, Briony Horgan

Chal target, sol 78

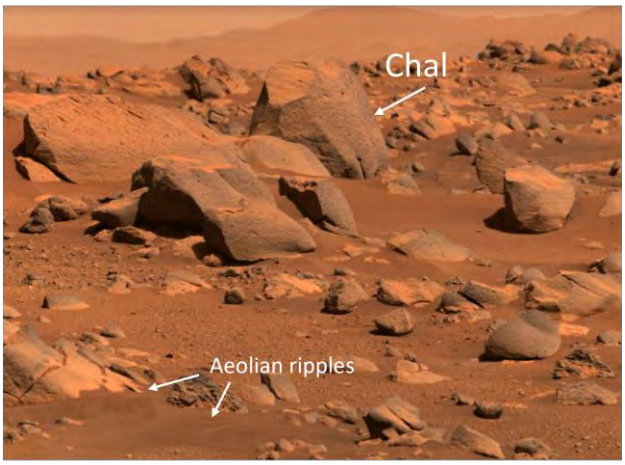

Sol 78, Seq. zcam03127, site 3, drive 2430, zoom 110

Sol 78, Seq. zcam03127, site 3, drive 2430, zoom 110

Fig. 20 – Left: Estimated true color image of Chal target using the L0 RGB filter. Right: Enhanced L0 RGB image of Chal target

Chal target (Figs. 7C; 20) is one of the later observations made while I was active in the Mastcam-Z downlink science support team. In this thesis I have chosen to present multispectral products created manually from this sequence, through methods presented in the methods sections. Since then, an automated process for producing multispectral parameter products, has been developed based on our manual efforts.

The Chal target is located in an area that is dominated by the two-toned massive rocks, although some pitted rocks can be observed in the foreground. The regolith appears to consist of relatively fine-grained material in places immediately next to large boulders, where aeolian ripples can be observed.

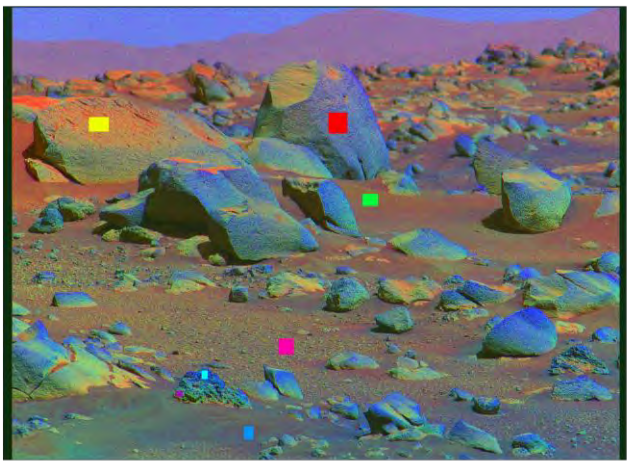

Sol 78, Seq. zcam03127, site 3, drive 2430, zoom 110

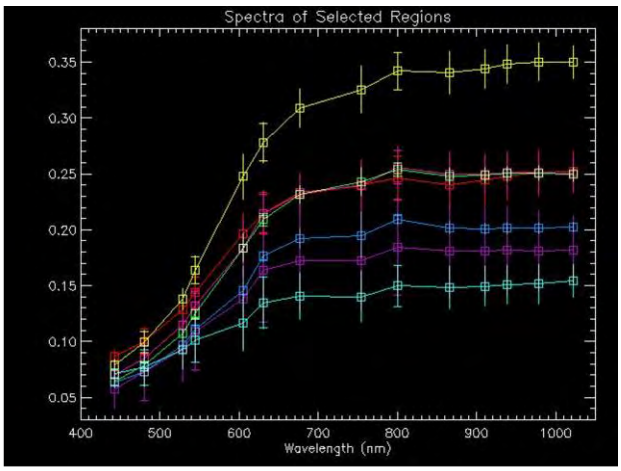

Fig. 21 – Left: Decorrelation stretch using filters L2 (754 nm), L5 (528 nm), and L6 (442 nm) with locations for spectra extraction highlighted. Right: Plots of the spectral properties of soils and rocks extracted from the image on the left.

In the Decorrelation stretch (DCS) (Fig. 21, left) we can see a clear diversity in the sediments. The coarse-grained material appears to be very heterogenous, with green/blue pebbles in a relatively red matrix. The fine-grained material in the foreground and next to Chal target look much more homogenous, although green/blue and red respectively. Looking at the spectral plots (Fig. 21, right) of the regolith (green/pink/blue) they share the same spectral signature in the infrared spectrum, but do have different slopes in the visible spectrum. The spectral signature of Chal (red) looks relatively similar to the regolith. They have a steep "red" slope in the visible spectrum, a peak near 750 nm and a long slope towards infrared. Although this is not too clear in the Chal target spectra (likely due to the heterogeneity of the extraction area), it is indicative of High-Calcium Pyroxenes (HCP), with Fe-bands centered near the end or beyond the capabilities of Mastcam-Z.

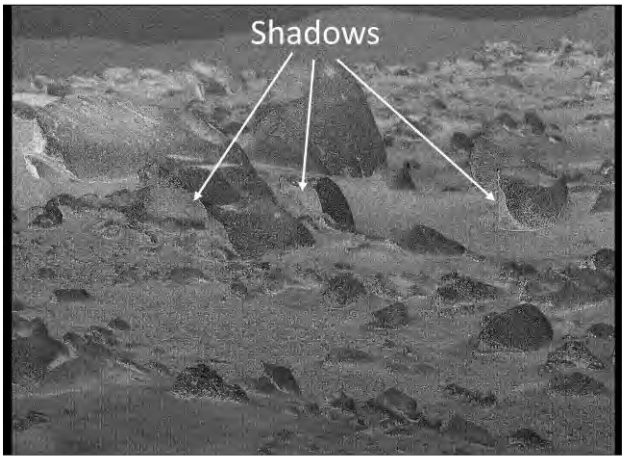

Sol 78, Seq. zcam03127, site 3, drive 2430, zoom 110

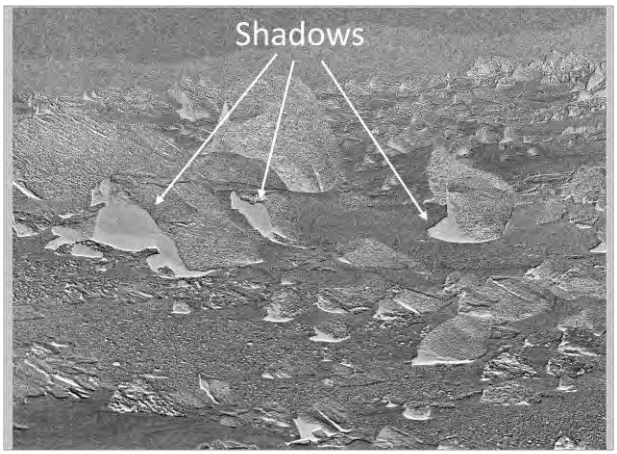

Sol 78, Seq. zcam03127, site 3, drive 2430, zoom 110

Fig. 22 – Left: Band depth map of Chal target using a band center at L5 (528 nm) and shoulders at L4 (605 nm) and L6 (442 nm). Right: Overall slope map in the infrared spectrum from R1 (800 nm) to R6 (1012 nm), with arrows pointing to shadowed areas.

The band depth map (Fig. 22, left) centered at 528 nm generally displays a strong band depth in the regolith and weak band depths in the massive rocks. A band center at 528 nm is sensitive to crystalline ferric phases, suggesting contents of hematite and other iron-oxides in the regolith (and dusty parts of the massive rocks). The photometric properties of this image disturbs the band depth map a bit, as shadows create a "false" strong band depth.

The near infrared slope map (Fig. 22, right) exhibits high values in the massive rocks, consistent with ferrous phases such as pyroxenes and olivines. The photometric properties of this image disturbs the slope map as well, as the shadows cast by the massive rocks create very steep spectral slopes. The steep slopes in the massive rocks are indicative of ferrous phases such as pyroxenes.

Máaz target, sol 12

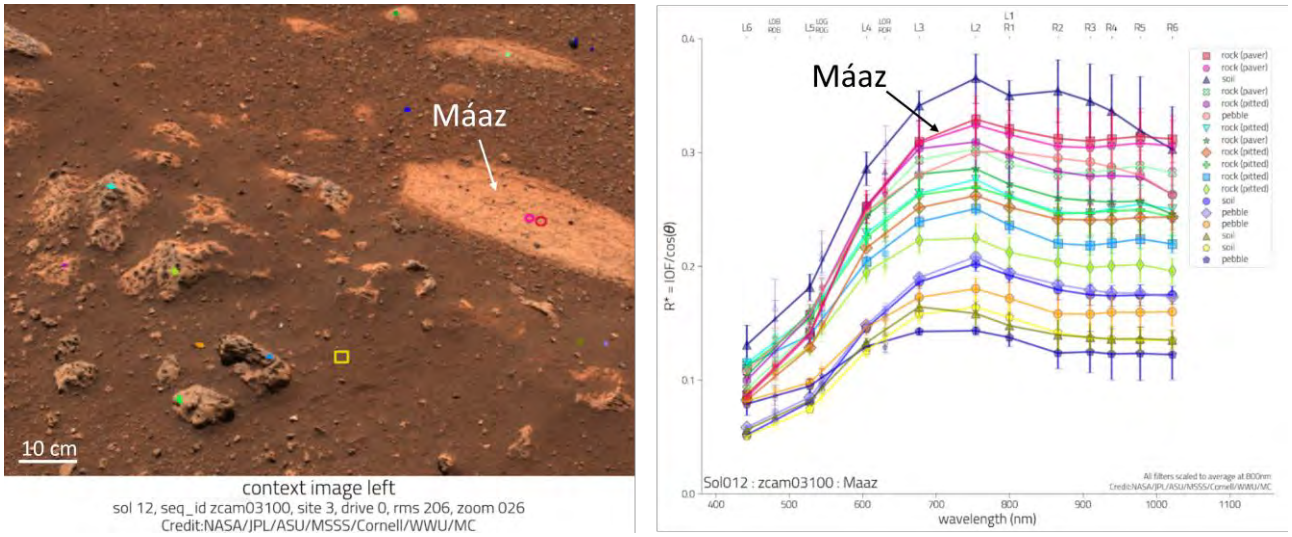

Fig. 23 – Left: Estimated L0 true color image of Máaz target with locations for spectra extraction highlighted. Right: Plots of the spectral properties of soils, pebbles and rocks extracted from the image on the left.

The first target for multispectral observation by Mastcam-Z, was a low-relief, light paver rock at the landing site named Máaz (Figs. 7C; 23, left). When looking at the spectra extracted from the image, we can see that the paver rocks, pitted rocks, soil, and pebbles have different spectral signatures (Fig. 23, right). One caveat is however, that the error bars in the spectra graphs due to small size or heterogeneity of the sample locations. As such the error bars does not represent a margin of error, but rather the standard deviation of any given sample. The pebbles naturally show the greatest variation in their spectral signatures, as they are likely sourced from different rocks, some of which might not even be present in the crater. The spectral signature of Máaz is consistent with LCP, with a steep "red" slope from 400–700 nm, a peak near 750 nm and a band center near 900 nm. The soil samples in the top right corner of Fig. 23 (left), both show a spectral signature consistent with HCP, again with a steep "red" slope, a peak near 750 nm and a long slope towards the Near-Infrared (NIR) spectrum.

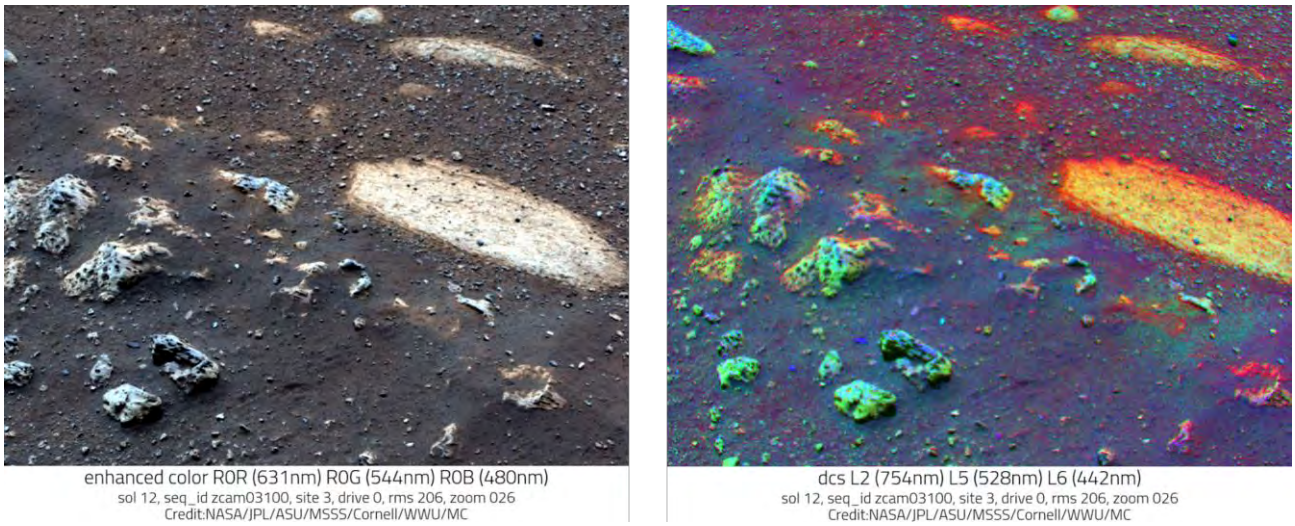

Fig. 24 – Left: Enhanced R0 RGB image of Máaz target. Right: Decorrelation stretch using filters L2, L5, and L6 of Máaz target.

The enhanced color image and DCS of Máaz (Fig. 24) show a clear spectral variation in the regolith and in the pitted rocks. In the DCS the pavers are characterized by a very strong orange color, and the pitted rocks are ranging from blue (at their tops) to orange (near the surface).

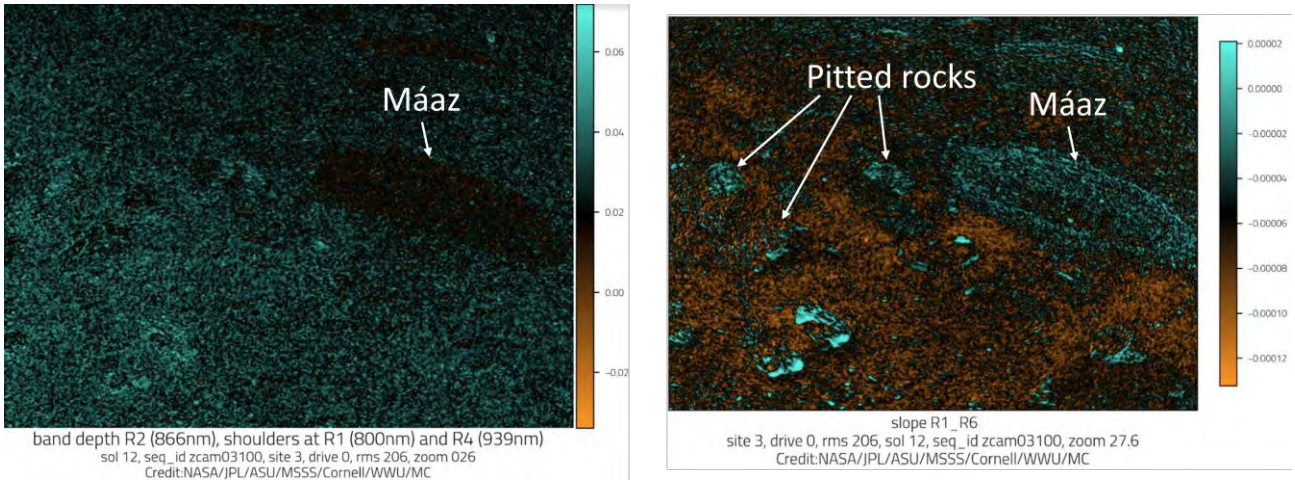

Fig. 25 – Left: Band depth map of Máaz target using a band center at R2 (866 nm) and shoulders at R1 (800 nm) and R4 (939 nm). Right: Overall slope map in the infrared spectrum from R1 (800 nm) to R6 (1012 nm).

The band depth and slope parameter maps (Fig. 25) shows distinct differences between most of the soil, the pavers, and the pitted rocks. In the band depth map with shoulders at 800 nm and 939 nm, Máaz (and pavers) are easily distinguishable as their spectral signature at 866 nm are relatively centered between the two shoulders, with slightly negative values consistent with pyroxenes. In the band depth map the regolith exhibits relatively high values consistent with

crystalline hematite or other iron-oxides. The near infrared slope map exhibits high values in the pavers, the pitted rocks, and some of the surrounding regolith, consistent with ferrous phases such as pyroxenes and olivines.

Yéigo, sol 16

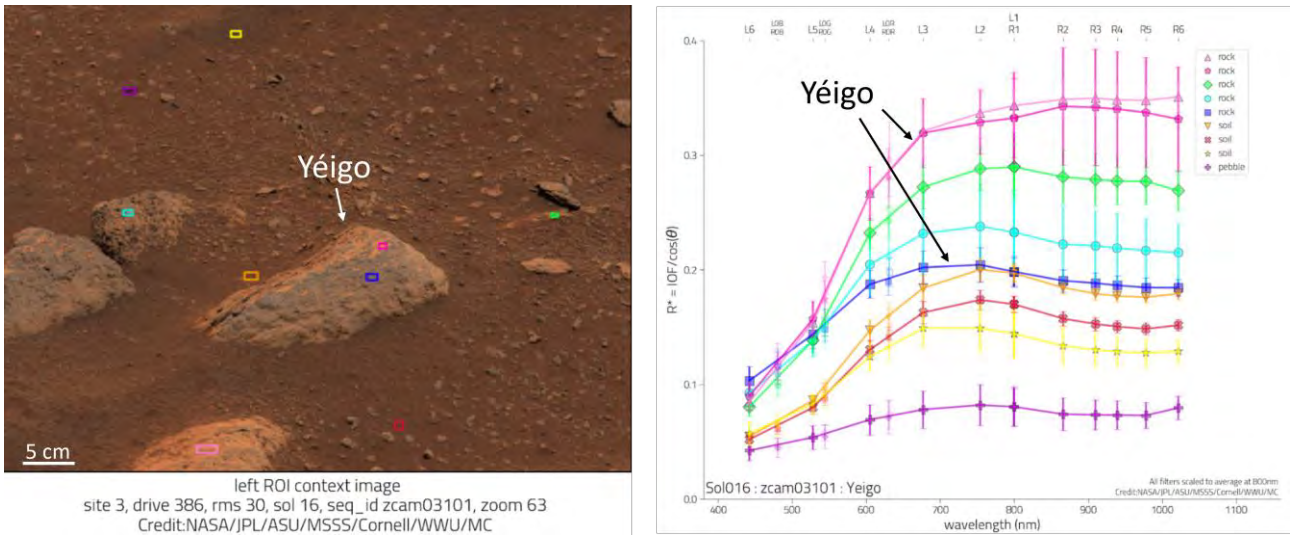

Fig. 26 – Left: Estimated L0 true color image of Yéigo target with locations for spectra extraction highlighted. Right: Plots of the spectral properties of soils, pebbles and rocks extracted from the image on the left.

Yéigo was the second target for multispectral observation (Figs. 7C; 26), only a short drive from the landing site. The spectral signature of Yéigo varies a lot between the two extractions in Fig. 26 (right), however the pink has some unusually large error bars, likely due to varying dust cover within the region of interest. The dark blue spectral signature exhibits a broad peak just below 700 nm and a long downward slope toward the near infrared. This signature is consistent with olivines, which exhibit Fe-bands centered beyond the spectral range of Mastcam-Z.

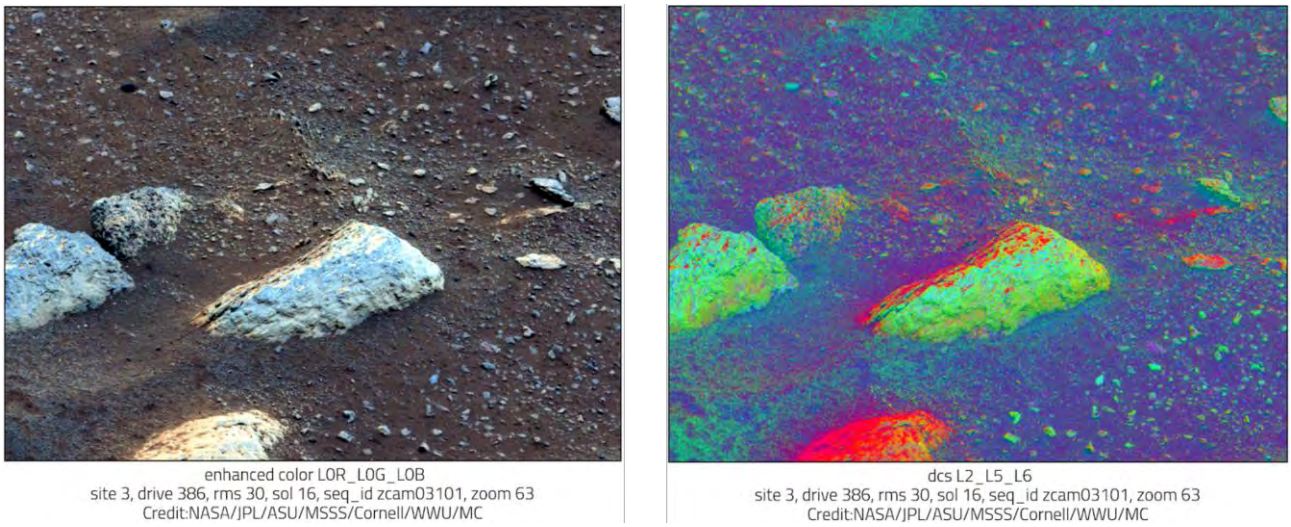

Fig. 27 – Left: Enhanced L0 RGB image of Yéigo target. Right: Decorrelation stretch using filters L2 (754 nm), L5 (528 nm), and L6 (442 nm) of Yéigo target.

Yéigo is difficult to classify as it is morphologically similar to the low-relief pavers but exhibits a different spectral signature. In the enhanced color image and DCS (Fig. 27), the top left part of Yéigo looks relatively similar to Máaz (Fig. 23). In the enhanced color image, the right-hand side of Yéigo looks much more blue. This could represent a continuum of differences in texture, weathering, and/or lithology of the same morphotype, possibly resulting in more erosion resistant higher-relief rocks.

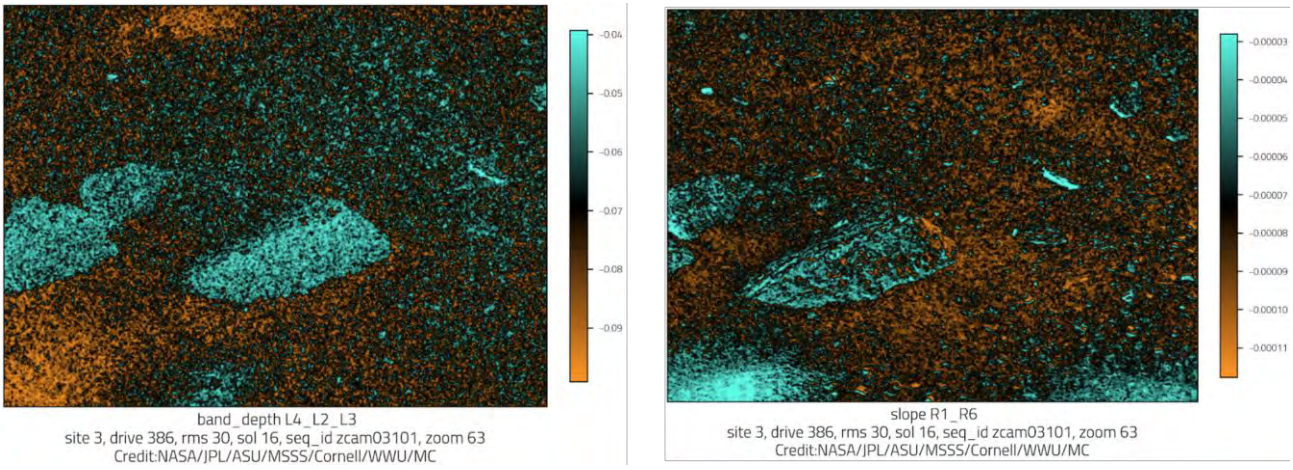

Fig. 28 – Left: Band depth map of Yéigo target using a band center at L3 (677 nm) and shoulders at L2 (754 nm) and L4 (605 nm). Right: Overall slope map in the infrared spectrum from R1 (800 nm) to R6 (1012 nm).

The band depth map (Fig. 28) exhibits relatively strong signals in Yéigo and the two rubbly rocks immediately to the left. The near infrared slope map exhibits high values in the same rocks. This is consistent with ferrous phases such as pyroxenes or olivines.

Íina, sol 28

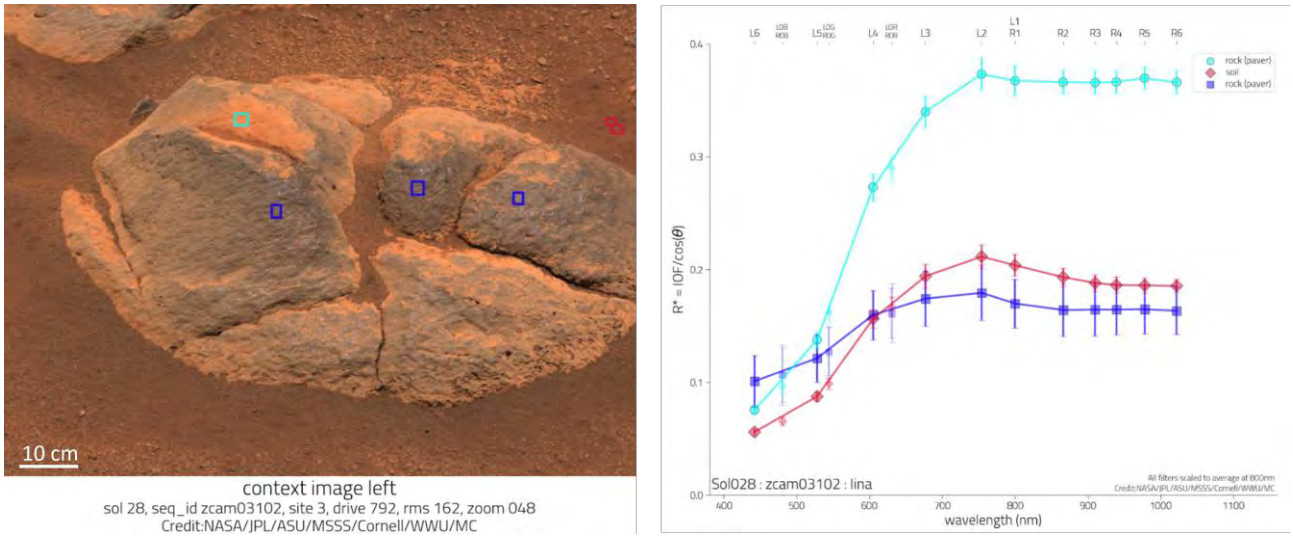

Fig. 29 – Left: Estimated L0 true color image of Íina target with locations for spectra extraction highlighted. Right: Plots of the spectral properties of soils and "clean"/dusty rock extracted from the image on the left.

The third multispectral observation was acquired on sol 28 of the Íina target (Figs. 7C; 29). Morphologically it appears to be different to both Máaz and Yéigo, but it carries a similar spectral signature to Yéigo. The soil surrounding Íina carries a spectral signature with a broad peak at around 700 nm and a long downward slope towards NIR consistent with olivine. The turquoise sample displays a spectral signature with a very flat NIR profile, likely attributable to dust cover and/or weathering.

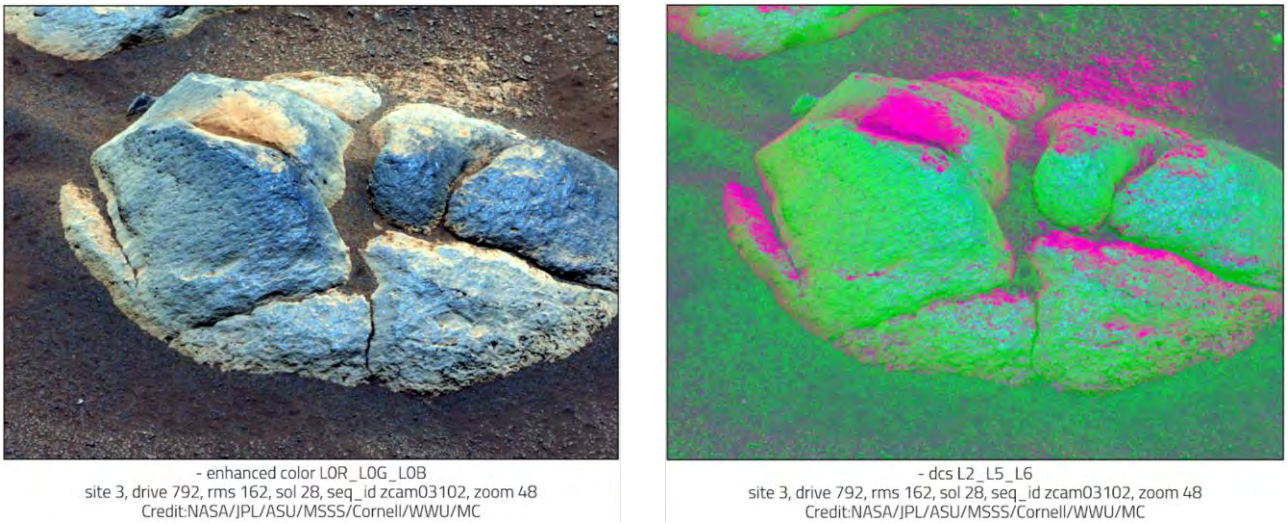

Fig. 30 – Left: Enhanced L0 RGB image of Íina target. Right: Decorrelation stretch using filters L2 (754 nm), L5 (528 nm), and L6 (442 nm) of Yéigo target.

The enhanced color image and DCS of Íina (Fig. 30) both highlight areas covered by dust, mainly in the fractures and the embedded rubbly rock surface in the background.

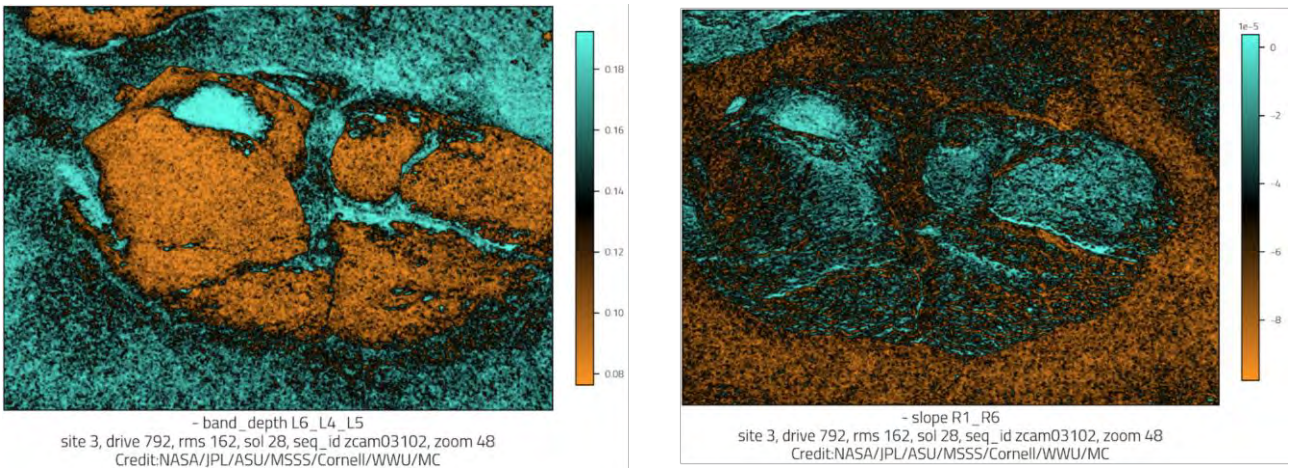

Fig. 31 – Left: Band depth map of Íina target using a band center at L5 (528 nm) and shoulders at L4 (605 nm) and L6 (442 nm). Right: Overall slope map in the infrared spectrum from R1 (800 nm) to R6 (1012 nm).

The band depth map centered at 528 nm (Fig. 31) has strong signals in the regolith surrounding Íina and in the fractures within the target. This is consistent with crystalline ferric phases such as hematite and other iron-oxides.

6.2.2 Rock distribution

The distribution of rock morphotypes at the Octavia E. Butler landing site (Fig. 7) is intermixed, but generally correlates with elevation (Fig. 32). The low-relief pavers are topographically lower than the massive rocks.

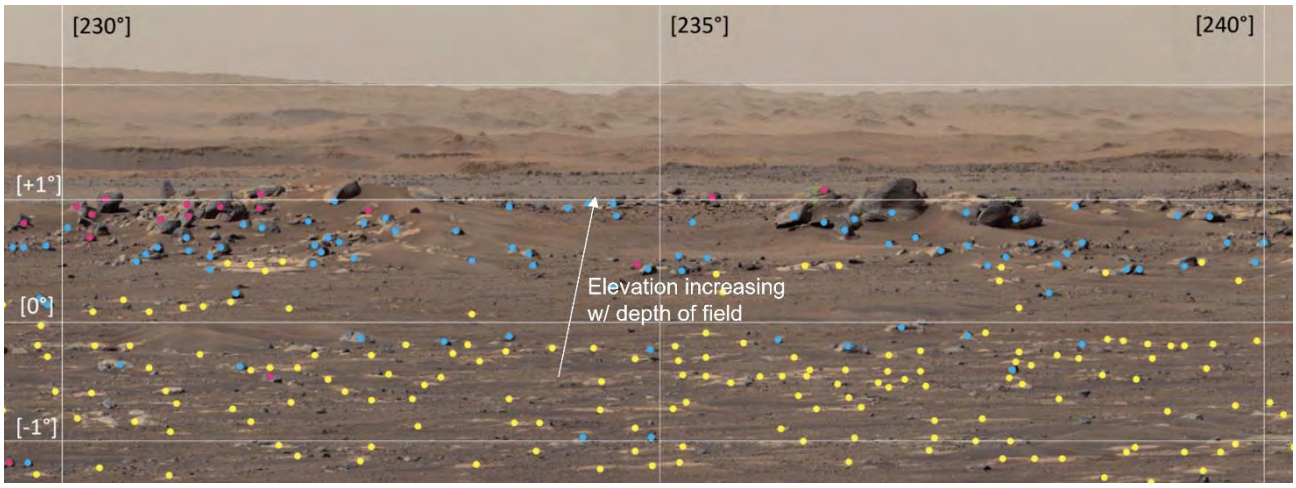

Fig. 32 – Cropped image from the sol 4, zcam00024, Z110 mosaic with rock morphotypes marked. Yellow = pavers, Blue/pink = massives. From: Linda Kah, sol 48 Science Discussion

6.2.3 Auto-focus analysis

Along the traverse of the rover, a common procedure is to acquire panoramic images with Mastcam-Z. These images are used to provide detailed morphology, topography, and geologic context for scientific targets and sample extraction locations. Unless manually specified by the uplink team, the images will be acquired with a set of automatic focus parameter settings, based on zoom settings and distance to target. As the rover deck and hardware are typically in the frames proximal to the rover, the distance between foreground and background is relatively large. This can cause complications when acquiring images with auto-focus parameter settings. This is the case for the first 360° panoramic image taken on sol 3, shown in Fig. 33.

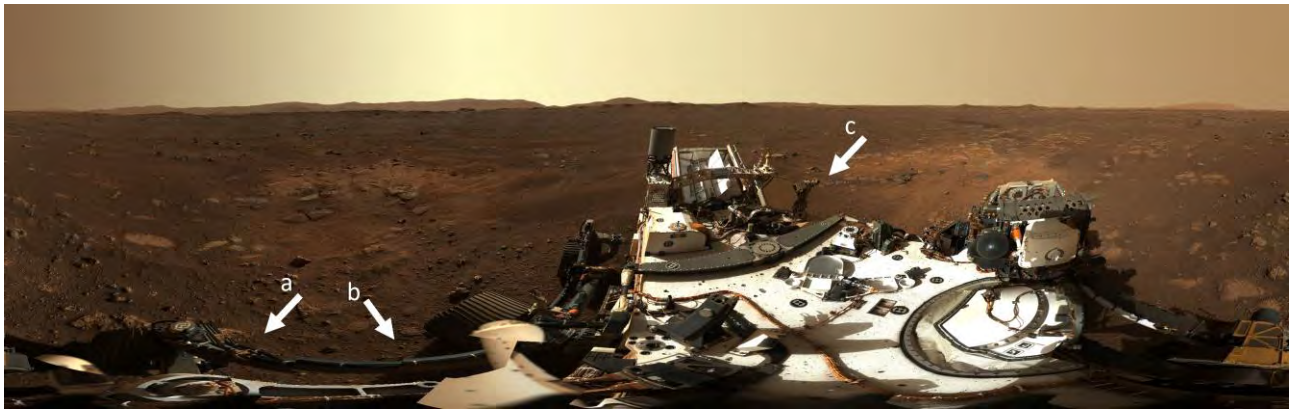

Fig. 33 – Full 360° left-eye panorama at 34 mm focal length acquired on sol 3 at the Octavia E. Butler landing site. White arrows point to areas that are out of focus shown in Fig. 34.

An identical panorama was reshot from the same location on sol 11 with manually adjusted focus parameters, effectively increasing the depth of field. As part of the Mastcam-Z science support

team, it was our task to look at these reshot frames and assess the volume of scientific data lost when using auto-focus parameters for panoramas including the rover deck and hardware. By systematically going through the two panoramas each consisting of 95 frames, we compared the visibility of textures and structures in the rocks and regolith. Examples of the results are shown in Fig. 34.

When looking at the image pairs, it is evident that more details are visible in the sol 11 images. As an example, Fig. 34a and 34b, include a pebble of bright pitted rock which structures are much more obvious in the sol 11 frames. The individual grains of the regolith are also easier to identify, and the diversity in color ranging from very dark to bright can easily be observed. The larger clasts of the regolith at the Octavia E. Butler landing site appears to be sourced primarily from the bright, pitted rocks and the low-relief pavers, although pebbles from the darker massive rocks are also present.

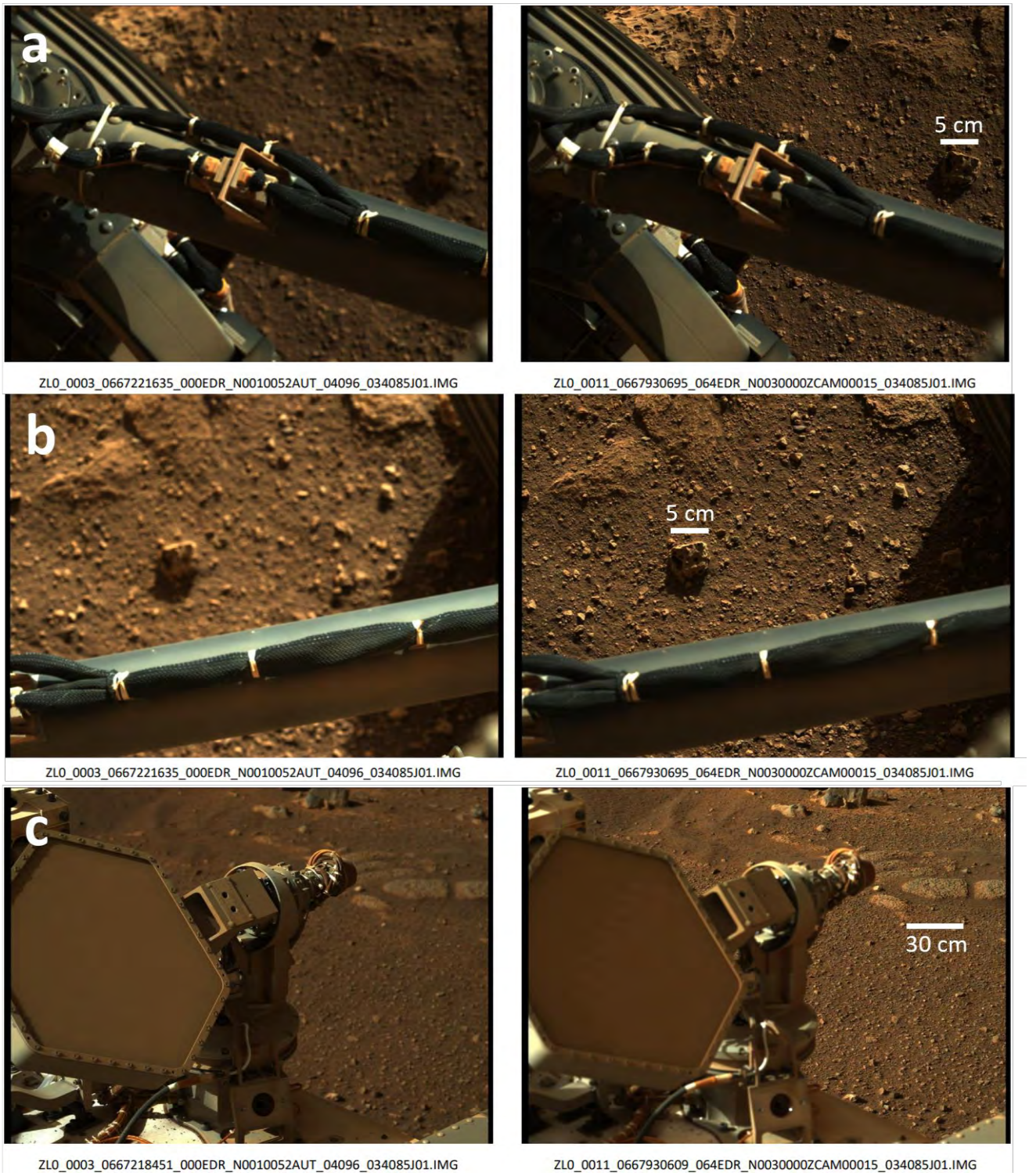

Fig. 34 – Parts of the sol 3 seq. 00013 panorama (left) and the sol 11 seq. 00015 panorama (right). The labels refer to the positions shown in Fig. 33.

6.2.4 Van Zyl overlook mosaics

The Van Zyl overlook is a location in the proximity of the Octavia E. Butler landing site (Fig. 7C) where the rover was parked for an extensive period, while Ingenuity demonstrated controlled flight on Mars. As Perseverance was going to be parked there for a while and with plenty of bandwidth, Mastcam-Z was tasked with detailed documentation of the area. A 10-part series of mosaics (1029 pointings in total) were laid out to cover as much area as possible (Fig. 35), at the largest (110 mm) focal length providing very high-resolution images of the surroundings of the rover. In addition to documenting the Van Zyl overlook, these mosaics were downlinked as lossy JPEG quality factor 85 files, to assess the significance of scientific data lost in compression of data files. As part of my work in the Mastcam-Z science support team, I contributed to the generation of the mosaics documenting the Van Zyl overlook (Figs. 36-38) and set up a spreadsheet for systematically going through all Van Zyl sequences in the search for JPEG compressional artifacts. The purpose of this test was to see if significant scientific data was lost in compression, or if future data files could be downlinked at a quality factor 85 – unless requested at lossless compression. The result was that lossy JPEG quality factor 85 compression did not compromise the scientific data within the images, unless the science of interest involved very thin laminae or fine-grained sediments.

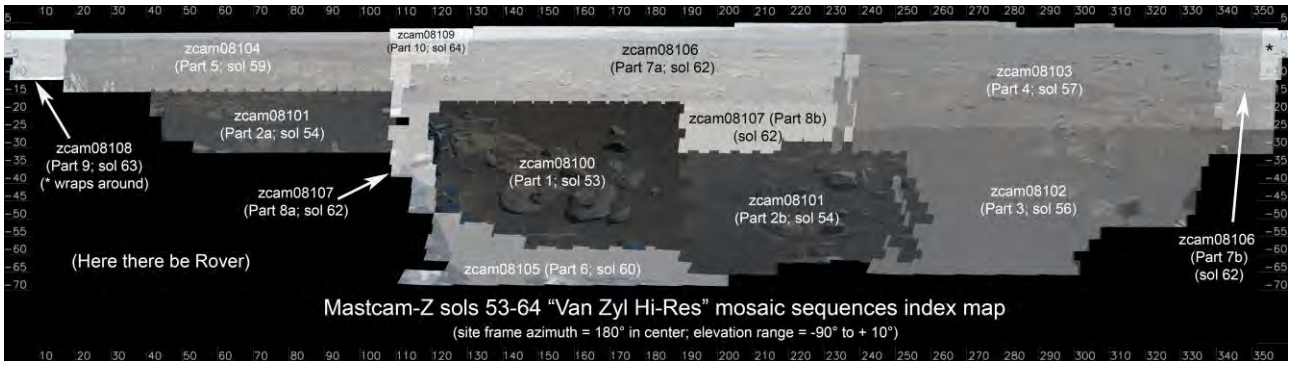

Fig. 35 – Index map of the Van Zyl overlook mosaics with keys to which sequences cover which terrain. From: Jim Bell, ASU

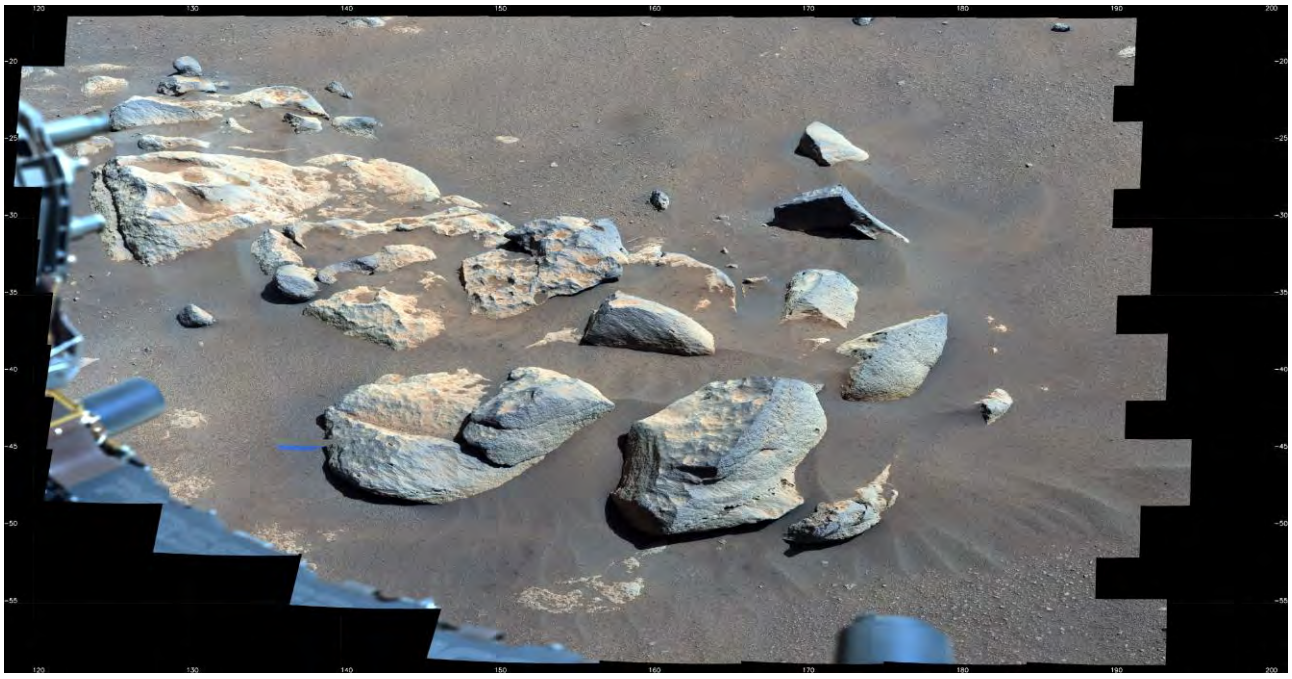

Fig. 36 – Part 1 of the Van Zyl overlook mosaic, sol 53, seq. 08100. This enhanced color mosaic is made using the L0 filter, 110 mm focal length, and consists of 124 pointings.

Fig. 37 – Part 2a of the Van Zyl overlook mosaic, sol 54, seq. 08101. This enhanced color mosaic is made using the L0 filter, 110 mm focal length, and consists of 60 pointings.

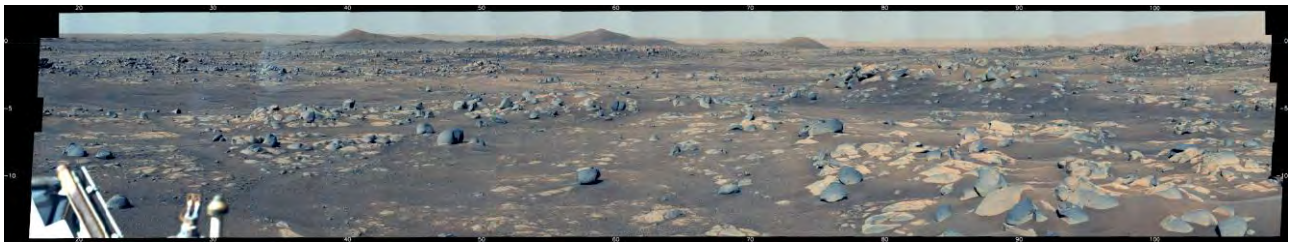

Fig. 38 – Part 5 of the Van Zyl overlook mosaic, sol 59, seq. 08104. This enhanced color mosaic is made using the L0 filter, 110 mm focal length, and consists of 89 pointings.

6.2.5 Long-term rover planning

To assess the stratigraphic ordering of the units present in Jezero crater, it is crucial to investigate unit boundaries. This includes boundaries between the Cf-fr unit and the delta-associated remnant deposits. Upon landing, the route for the primary mission was still up for debate, as the exact landing site (within the landing ellipse (Fig. 7)) was unknown. Mastcam-Z was tasked to contribute to a discussion purposed to guide the choice of the long-term rover planners, whether we should continue clockwise or counter-clockwise around the southern part of Cf-f-1 (Section 3.2.1), also named Séitah. The decision was based on the diversity of scientific potential versus distance and traversability of the rover. Mastcam-Z is a camera with long-range capabilities and as such we organized two groups to analyze our observations, and present arguments for each route (Fig. 39). The counter-clockwise route is longer if the eastern remnant complex is included, but is a relatively simple traverse. The clockwise route is shorter but a more complicated traverse and includes the Kodiak remnant close to the southern delta scarp.

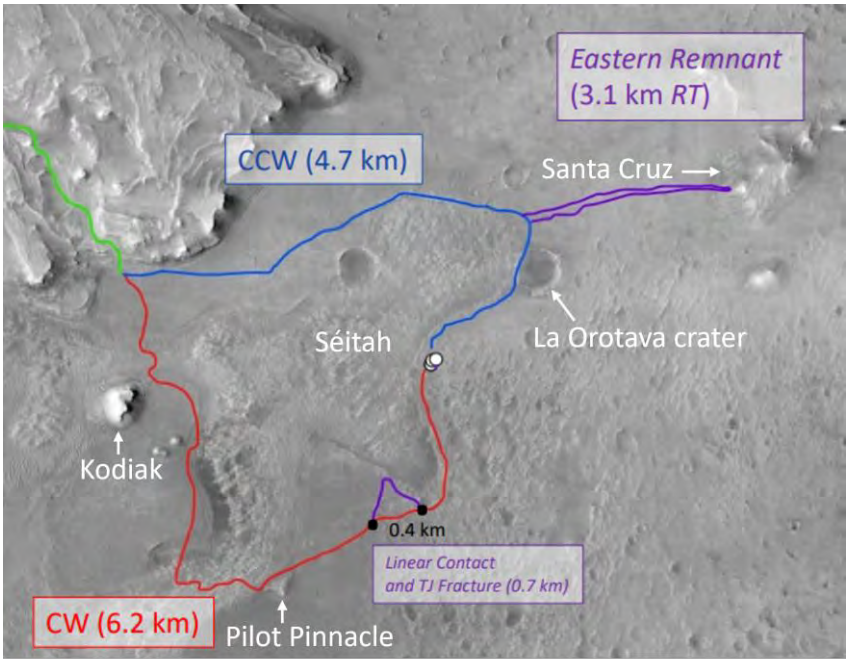

Fig. 39 – Preliminary routes suggested for the primary phase of the M2020 mission.

My participation in the delta-associated remnant deposit discussion was mainly with the eastern group, although I did participate in both. In the eastern delta-associated remnant deposit group we argued that the Santa Cruz (Figs. 40; 41) remnant was of most scientific interest, as it contains parts that appear morphologically similar to the two other delta-associated remnant deposits: Isle Royale and Mauna Kahalawai (Fig. 41). First we wanted to investigate how much of Santa Cruz was visible from the landing site, in particular if the base of the remnant was

visible. For that purpose, I highlighted key features from orbital data and compared with ground images from Mastcam-Z and extracted an estimated elevation profile of the southern part of Santa Cruz, in an attempt to estimate an approximate viewshed of the remnant (Fig. 40).

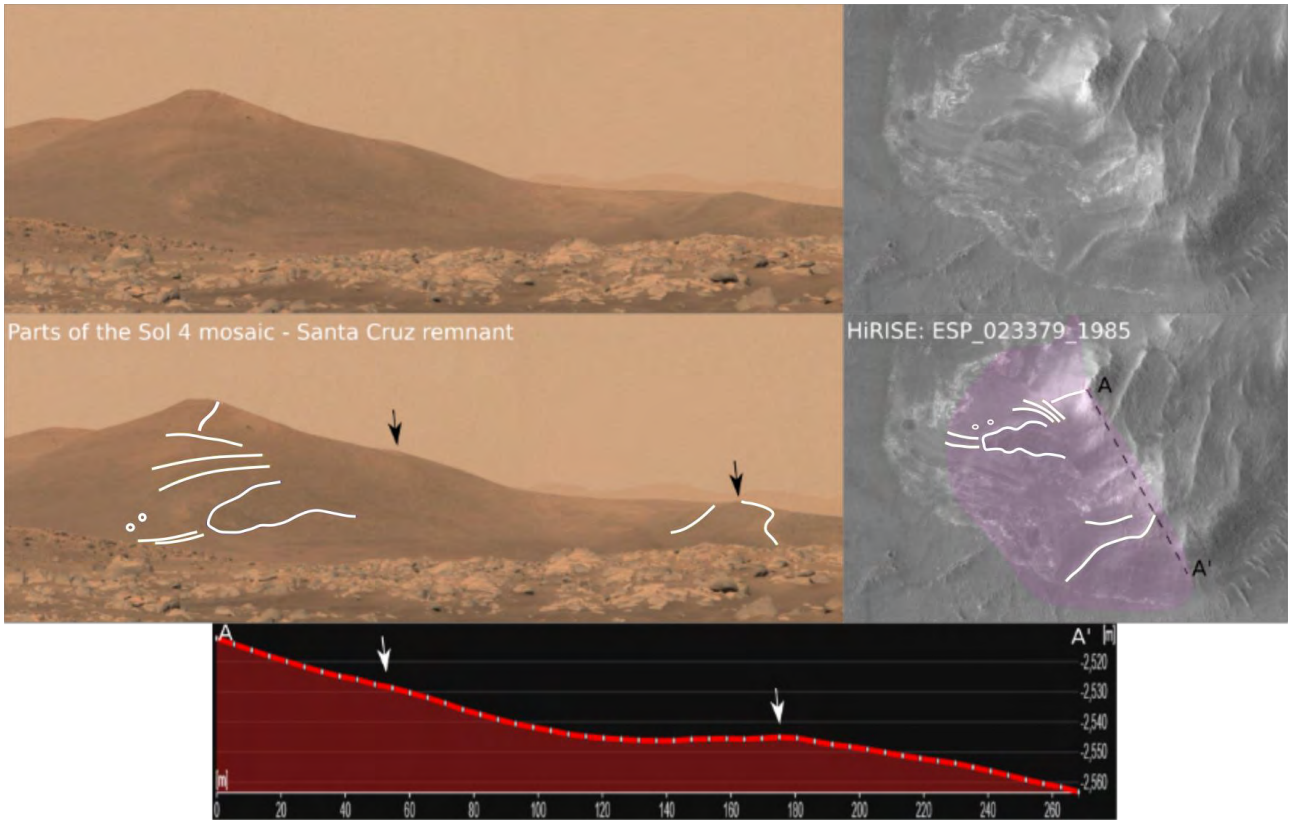

Fig. 40 – Comparison of Mastcam-Z (sol 4, seq. 00024) and HiRISE data in an attempt to estimate an approximate viewshed of Santa Cruz from the Octavia E. Butler landing site. The distance from rover to Santa Cruz is approximately 2.5 km. Top: Raw images; Center: Images with features highlighted in white and estimated viewshed in purple; Bottom: Elevation profile of the southern ridge of Santa Cruz.

The key selling points for choosing the counter-clockwise route were that we would reach a unique location in the La Orotava crater (Fig. 39). It is a crater with most of the eastern rim exposed, allowing for observations under the surface which otherwise is out of reach. Another reason to go for the counter-clockwise route is to reach a delta-associated remnant deposit more distant to the delta scarp. These distal deposits would likely be composed of the most fine-grained silt and clay sediments (i.e., lacustrine mudstones) that we would have access to in the entire mission. These sediments would have been deposited by suspension in the deeper, quieter low-energy waters with excellent preservation potential for any biogenic materials and provide crucial evidence for reconstructing the paleo-lacustrine history of Jezero crater.

Fig. 41 – Mastcam-Z 8x1 Z110 enhanced color mosaic of the eastern remnant complex, sol 38, seq. 08009. The eastern remnant complex is 2.4-2.8 km from the rover location, with Mauna Kahalawai being nearest.

The clockwise route (Fig. 39) also contains a distal remnant, Pilot Pinnacle which in orbital data appears to have a relatively exposed contact with the crater floor. Additionally Pilot Pinnacle is relatively flat (approximately 15 m above crater floor level) and likely more accessible for rover investigations. The traverse also provides good opportunities for exposed unit boundaries of all units on the crater floor.

To the west of Séitah is a remnant proximal to the delta scarp. Kodiak (Fig. 42) appears to contain a wide range of exposed deltaic strata, including planar parallel bedded strata (topsets) and inclined strata (delta foresets) (Mangold et al., 2021).

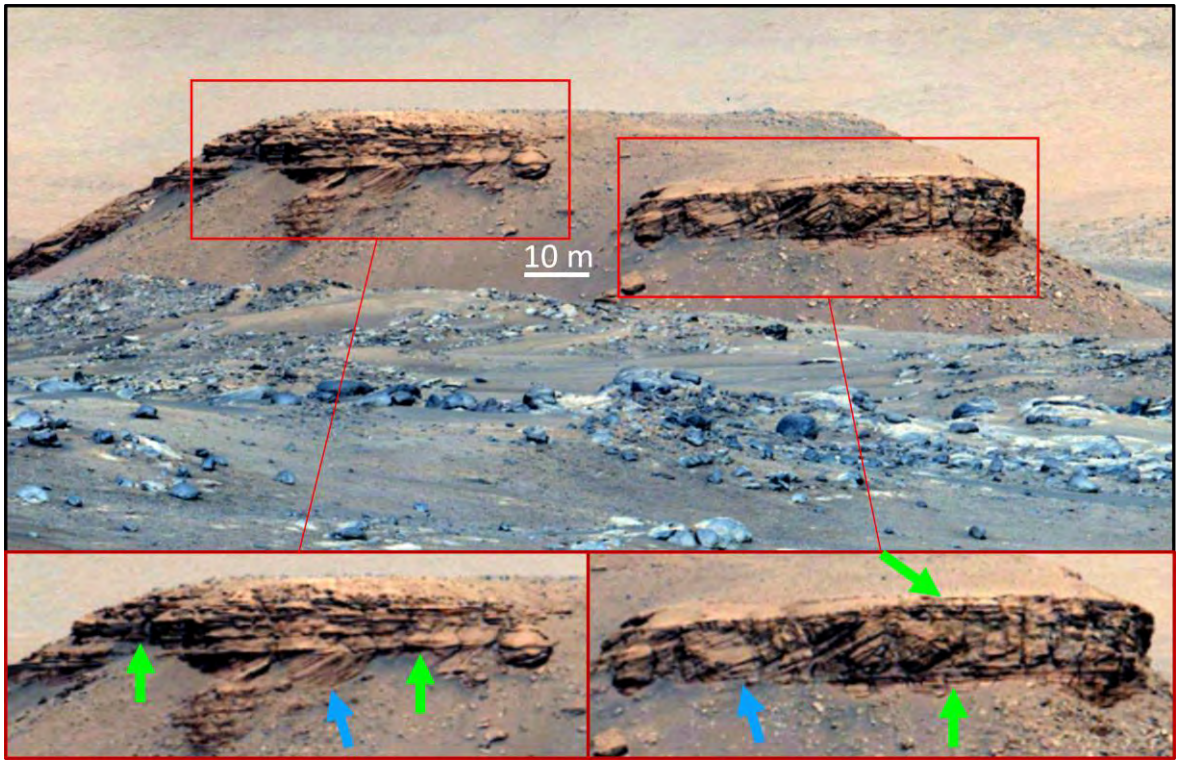

Fig. 42 – Top: Enhanced RGB Z110 image of Kodiak from sol 69, seq. 03120. Bottom: Zoom ins of exposed deltaic strata. Green arrows point to planar parallel beds. Blue arrows point to inclined strata. Distance from rover location is approximately 2.3 km

Instead of selecting the CW or CCW route, a decision to go for a temporary campaign was made. The crater floor campaign includes initially heading south from the landing site to investigate and sample outcrop targets, including Cf-fr and Cf-f-1 (Séitah). At the conclusion of the crater floor campaign, Perseverance will return to Octavia E. Butler Landing site and then traverse towards its next science campaign, in a CCW direction around Séitah. Following the crater floor campaign, Perseverance will continue north to La Orotava crater following the shorter blue route to the delta (Fig. 39), unless something of scientific importance is observed on Santa Cruz in the meantime.

6.2.6 Crater floor campaign and Séitah

Séitah is one of the targets of the crater floor campaign (Fig. 7). The primary goals of this campaign are to explore the lithology of the crater floor and establish its stratigraphic context.
This includes investigating the contact between Cf-fr, Us and Cf-f-1 (Séitah). Séitah is a prominent inlier unit that sits between the landing site location and the delta scarp. Upon reaching the southern part of Séitah on sol 202, Mastcam-Z made a two-pointing observation towards the Cf-f-1/Cf-fr boundary south-southeast of the rover (Fig. 43). The location features very distinct layering in the bedrock, unlike the more erosion-resistant material of the Cf-fr-Us. Although this part of the unit boundary does not have a very prominent moat in my topographical map (Fig. 15), a local topographical depression can be observed from the ground (Fig. 43). The layered units on either side of the moat appear to be dipping towards south. The layers have recently been proposed (by the RIMFAX team) to be parts of Séitah that have been exposed due to erosion of Cf-fr and are interpreted to be delta foresets. This would make for a very mafic delta, given Séitah's strong olivine spectral signature.

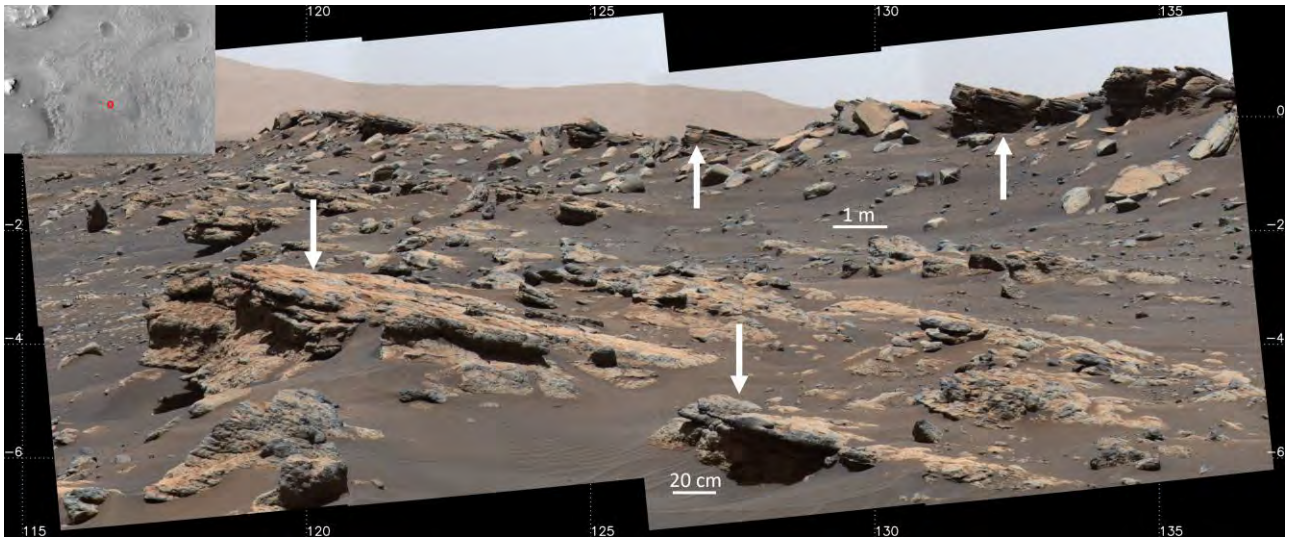

Fig. 43 – Eight-pointing mosaic from sol 202, seq. 08224 of the Séitah boundary region. White arrows point to areas with distinct layering. Rover location is shown in the top left. The visible local depression is within the Cf-f-1 (Séitah) unit, bounding with the Cf-fr unit behind the ridge (right hand side in this mosaic).

7. Discussion

7.1 Origin of the Cf-fr and Us units

Early work by Schon et al. (2012) and Goudge et al. (2015) interpreted the Cf-fr unit to be a basaltic lava flow that resurfaced the Jezero floor. This interpretation was primarily based on visual similarities, e.g., dark tone, high crater retention, and layered lobate margins, to lava flows elsewhere on Mars. The major argument against this hypothesis is that the Cf-fr is highly topographically variable over large scales and does not create an obvious flow surface (Horgan et al., 2020). Recent observations made by the Curiosity rover and HiRISE images of Gale crater, have shown that well-cemented sandstones (Edgett and Malin, 2014) and well-cemented mudstones (Calef et al., 2019) can retain many sub-kilometer-scale impact craters. Thus, fluvial origin is also a plausible interpretation for the Cf-fr unit. This is consistent with the inclination of Cf-fr presented in my topographical profiles (Fig. 16), which is similar to the slope of the upper surface of the western delta. The slope direction of the upper surface of the delta and Cf-fr is different from the general slope of the crater floor in Jezero, which is preferentially from north to south rather than east to west (Fig. 44). The slope of Cf-fr is inclined along axes that appear to be radial to the delta, rather than uniform across the unit. This could be indicative of Cf-fr sharing a

common origin with the delta, although processes depositing material mantling existing topography could also be consistent with this observation. By looking at CRISM data (Fig. 17) the Cf-fr is the only unit in Jezero crater that carries an HCP signature, meaning that the material does not likely have a source within Jezero crater. The HCP-bearing composition of Cf-fr is consistent with more evolved magma compositions often associated with Hesperian and Amazonian volcanics (Horgan et al., 2020). The HCP signal, while unique to the Cf-fr unit in Jezero crater, is observed as the main spectral signature of a regionally extensive mantling unit outside of Jezero crater (Goudge et al., 2015). This could suggest that the Cf-fr unit is sourced from aeolian or fluvial reworking of this regional basaltic mantling unit, resulting in a sedimentary rock of basaltic composition.

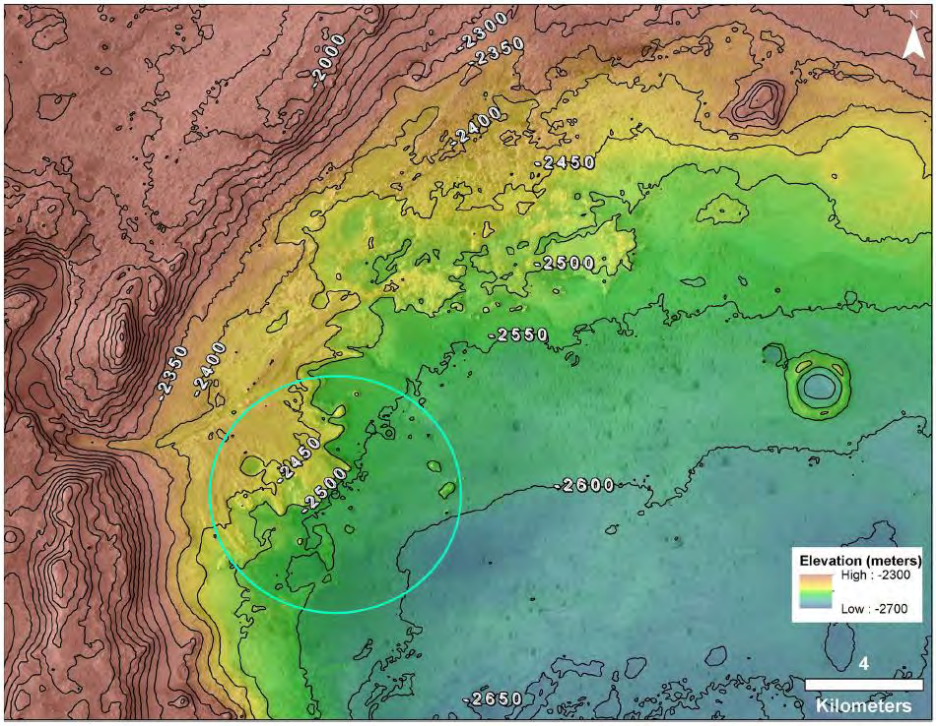

Fig. 44 – Topographic map of the northwestern part of Jezero crater showing the slope direction of the crater floor and the landing ellipse of the Mars 2020 mission. From: Holm-Alwmark et al., 2021

The dark tone that was previously associated with Cf-fr, is now associated with a variable superposition of the Us unit. In areas with thinner surficial cover, the Cf-fr exposures are lighter in tone (Stack et al., 2020). This variation in thickness of surficial cover also results in variable muting of underlying features such as crater rims and fractures. The crater retention of Us is very poor and exhibits few small meter-scale craters (Stack et al., 2020). The occurrences of Us in Jezero crater are primarily exposed near the western delta scarp and could be lags left from

erosion of friable layers within the deltaic sequence. The occurrences and distribution of Us could thus indicate a potential past extent of the western delta fan (Fig. 7).

7.2 Units represented in rock morphotypes

By comparing the spectral signatures of the rocks I have presented in the results section to CRISM data, a potential source of origin can be hypothesized. Chal (Fig. 20) is a massive rock with a strong HCP signature, spectrally similar to the regional basaltic mantling unit. As Cf-fr is the only unit in Jezero crater with a HCP signature, Chal and other massive rocks are likely sourced from Cf-fr. The regolith, at the Octavia E. Butler landing site, also carries the same HCP signature and is likely sourced from erosion of the topographically higher massive rocks. Erosion of the layers containing massive rocks at the landing site leaves the low-relief pavers exposed, which carries an LCP signature. The LCP signature in the pavers, e.g., Máaz (Fig. 23), is consistent with the LCP signature of the delta, suggesting a deltaic source of origin. The massive rocks are likely a result of transportation of boulders during a highly energetic fluvial phase, embedded into Máaz-like mudstone eroding out of it and dominating the erosional lag.

7.3 Stratigraphic relations in Jezero crater

The stratigraphic relations between geologic units in Jezero has been widely debated for years. The earliest detailed studies of Jezero crater suggested that the crater floor units (Cf-fr and Us) were emplaced after deltaic activity (Schon et al., 2012; Goudge et al., 2015 (Fig. 45). This stratigraphic interpretation was based on the apparent embayment of the western and northern delta fans. More recent studies suggest temporal relationships between the geologic units in Jezero crater, including hypotheses that suggest the crater floor units pre-date deltaic deposition or at least the later stages of fluvial activity (Holm-Alwmark et al., 2021). Stack et al. (2020) presented four scenarios for the stratigraphic relations of Jezero crater (Fig. 45), one of which (Scenario 3) is consistent with previous work by Goudge et al. (2015). The remaining three scenarios (1, 2, and 4) require different depositional relations between the Jezero delta and other crater-fill units. For the spatial extent of the units presented in each scenario, see Stack et al. (2020).

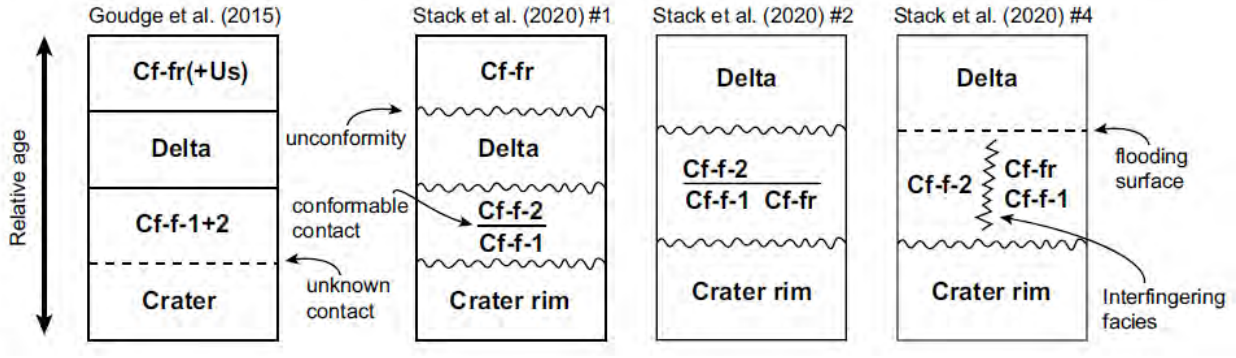

Fig. 45 – Hypotheses for the stratigraphic relations between geologic units in Jezero crater presented by Goudge et al. (2015) and Stack et al. (2020). From: Holm-Alwmark et al., 2021.

Scenario 1

In scenario 1 (Fig. 45, column 2) the Cf-f-1 and Cf-f-2 units are shown as a conformable sequence deposited in time order according to their respective elevations and are likely coeval with the regional fractured unit in Nili Planum outside of Jezero crater. In this scenario the deposition of the Jezero delta is considered to be a single depositional sequence for relative simplicity and is deposited unconformably on Cf-f-1 and Cf-f-2. Following the draining of Jezero crater lake and erosion of the delta to its present-day extent, deposition of the Cf-fr unit would have occurred, embaying the delta, delta-associated remnant deposits, and exposed outcrop of the underlying Cf-f-1 and Cf-f-2 units. Finally, the deposition of the Us unit and recent aeolian bedforms completes this scenario (Stack et al., 2020).

Some of my results of this thesis, and in particular Fig. 32, are consistent with this scenario. Massive rocks with HCP signatures, spectrally associated with evolved magma compositions, are located topographically higher than the low-relief pavers with LCP signatures (Fig. 32). This suggests that the later stages of fluvial activity could have reworked and transported the relatively young Hesperian/Amazonian evolved volcanic material, which is regionally mantling the area surrounding Jezero crater.

The lack of moats at the contact between the delta and Cf-fr (Figs. 15; 16), presented in the results section contradicts this scenario, as the lack of moats is indicative of the Cf-fr unit predating the delta. An explanation could be the erosional rate of the Cf-fr keeps pace with or outpaces the delta, preventing the formation of a moat. Another possibility is that Cf-fr is a fluvial unit interspersed in the delta, deposited in a flooding event before the later stages of delta deposition.

Scenario 2

Scenario 2 (Fig. 45, column 3) is similar to Scenario 1 with Cf-f-1 and Cf-f-2 being a conformable sequence possibly coeval with the regional fractured unit in Nili Planum outside of Jezero crater. In this scenario the delta is overlain on the Cf-f-1 and Cf-f-2 like in Scenario 1, but Scenario 2 also includes the Cf-fr unit in the same depositional sequence as the fractured units, based on textural and tonal similarities between the Cf-fr and Cf-f-1/Cf-f-2, and exposures of Cf-fr and Cf-f-1 at the same elevation range (Stack et al., 2020).

Scenario 4

Scenario 4 (Fig. 45, column 4) suggests the delta and Cf-f-1/Cf-f-2 units as the same depositional sequence with no major unconformities within it. Like in Scenario 2, the Cf-fr unit is considered part of the Cf-f-1 unit, but the relationship with Cf-f-2 is time equivalent and interfingering, rather than units deposited in succession as in Scenarios 1 and 2. This scenario recognizes the significant unconformity between the crater rim bedrock and the crater fractured units. However, despite some erosion occurring at the flooding surface between the delta and crater fractured units, the relative time of this erosional surface is significantly less, than the major unconformities as a result of exposed bedrock (Stack et al., 2020).

7.3.1 Moats

The presence or absence of topographic depressions at unit contacts, i.e., “moats”, describes the differential erosion of adjacent geologic units. When higher-standing relatively less resistant material is eroded at the contact of an embaying unit of higher resistance a moat appears. This is a result of the topographically higher-standing material eroding at a higher rate, than the adjacent younger and more resistant material. Ruff (2017) draws an analogue to Jezero crater from Columbia Hills in Gusev crater with focus on moats and “kipukas”. Kipukas are islands of older, higher-standing material embayed by a younger and more resistant material. The term kipukas implies not only the stratigraphic relation between the two units, but also a geologic origin (i.e., a lava flow) of the embaying unit, which is not necessarily the case in Jezero crater. As mentioned, the Cf-fr unit may be the deposition of fluvial reworking of basaltic material surrounding Jezero crater.

By looking at my topographical profiles (Fig. 16) it is quite evident there are no moats at the delta scarp/Cf-fr and delta-associated remnant deposits/Cf-fr boundaries. The lack of moats

at these contacts can be explained by the relative age of the delta being younger than the Cf-fr (Fig. 45, scenario 2 and 4). Another explanation could be the erosional rate of the Cf-fr keeps pace with or outpaces the delta/delta-associated remnant deposits, although this seems highly unlikely, as we would expect exposed deltaic surface.

7.4 Origin of delta-associated remnant deposits

The origin of the delta-associated remnant deposits is still debated, in particular the eastern delta-associated remnant complex (Fig. 15, B-E). Based on their spectral signature in CRISM data they can be associated to the formation of the delta, but whether they are deltaic or lacustrine deposits is unclear. The delta-associated remnant deposits display a range of morphological expressions. Deposits A and F (Kodiak), that are proximal to the delta, displays clear internal stratification (Fig. 15, A and F). The internal stratification in Kodiak consists of both planar parallel beds and inclined strata (Fig. 42), likely representative of topsets and foresets in a prograding delta succession. The early observations made on Kodiak are discussed further in Section 7.4.1, in reference to a recent paper by Mangold et al., 2021. Deposits B-E located further east also display internal stratification but show less structural diversity and they appear to be more muted, which could indicate that they are of a finer grained material. An argument for a past extent of the western delta, reaching as far as the eastern remnant complex (and a deltaic origin of the remnants) could lie in the uppermost layer of the delta. Late highly energetic fluvial activity has deposited a layer of relatively large boulders visible on top of the delta fan and on Kodiak. These large boulders could have affected the erosional rate of the underlying material. If the boulders did not reach as far as the eastern remnant complex and did not provide a protective cover, it could explain the morphological differences in the remnants. To me, the lack of structural diversity and the muteness indicate that the eastern remnant complex are lacustrine of origin, rather than deltaic.

7.4.1 Kodiak by Mangold et al., 2021

Mangold et al., 2021 released the first paper after the landing of the Perseverance rover. The paper analyzes images taken by the rover in the first three months after landing in great detail, including observations made on the delta-associated remnant deposits.

Kodiak consists of two outcrop sections exhibiting five distinct stratigraphic bodies designated k1-k5 (Fig. 46), designated by Mangold et al., 2021. Unit k1 consists of plane-parallel horizontal to low-angle thinly bedded strata, overlain by steeply inclined beds with apparent southward dips at angles up to 35°. Another unit of dipping strata (k2) immediately overlies the uppermost strata of k1. Unit k3 shows similar geometries to those in k1, with thinly bedded, gently dipping, horizontal strata passing upwards into a distinct section of apparent southward dipping beds. Overlying the inclined beds of k3, across a sharp truncation surface is k4, which shows low-angle to locally cross-stratified subhorizontal strata. Unit k5 erosionally truncates k4 and consists of unsorted conglomerates, which contain boulders up to 1.5 m in size, implying a distinct change in depositional regime. The delta is interpreted by Mangold et al. (2021) to be a Gilbert-type delta, in which topset strata are fluvial deposits formed in delta top environments. The foreset strata represents deposits formed by gravity-driven flow processes on steeply dipping delta fronts. The bottomset strata represent finer-grained sediments deposited in areas immediately lakeward of the delta front (Mangold et al., 2021). The foreset orientation indicate an apparently southward progradation in this part of the western delta fan, during episodes of stationary or slowly decreasing lake levels. The truncation between k3 and k4 may represent a relatively sudden drop in lake level, leaving the foresets exposed to erosion. The bases of k1 and k3 at -2500 and -2490 respectively corresponds to the past lake levels at the time of deposition, and the stacking of units k1-k3 indicates an overall lake level rise of ~10 m before the truncation of k4. The diversity in geometries of Kodiak is thus indicative of delta growth into a lake system with fluctuating lake levels.

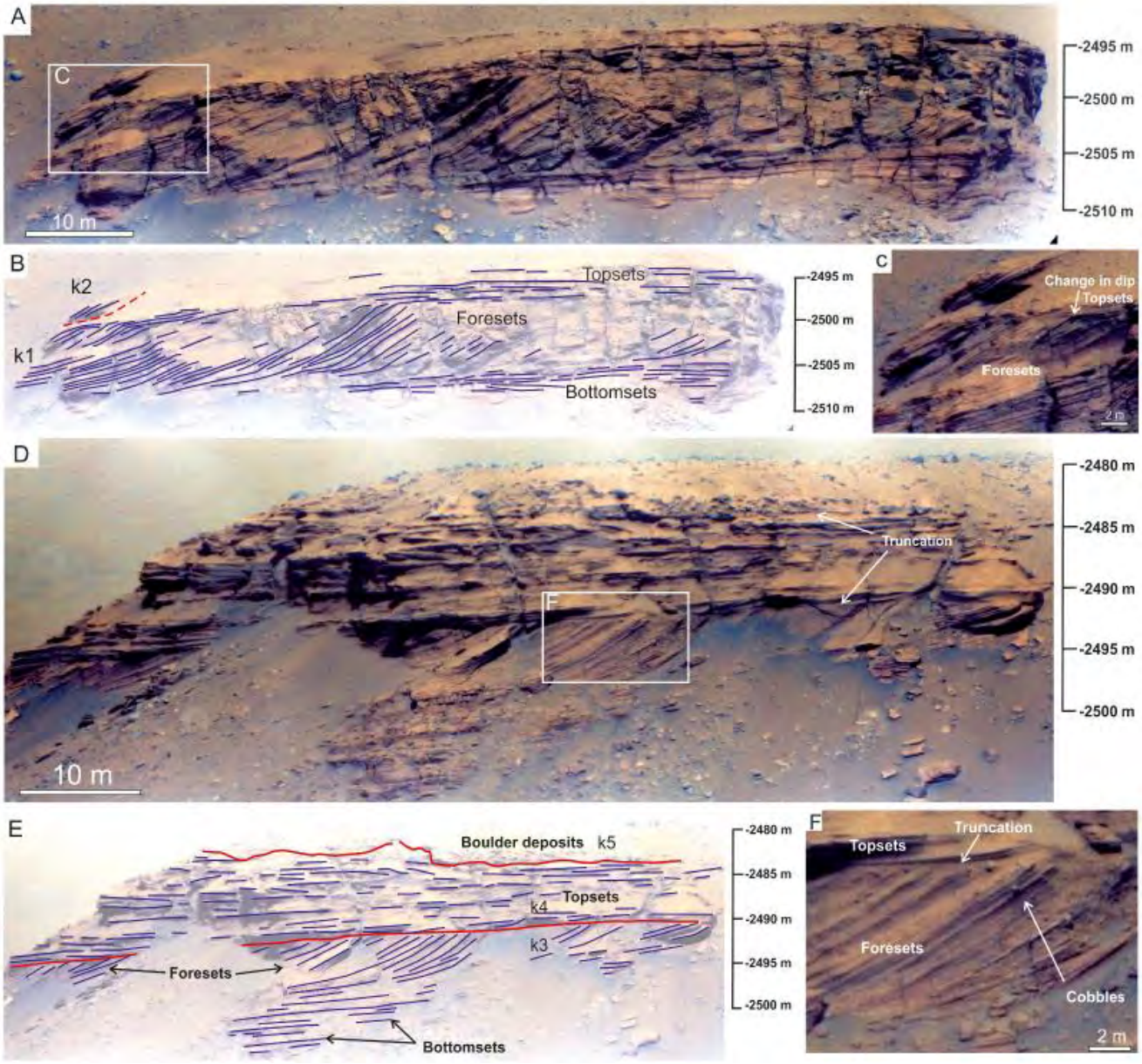

Fig. 46 – Stratigraphy of Kodiak. (A and D) Zoomed images of the two scarps of Kodiak. (B and E) Interpreted line drawings of the main visible beds (blue lines for individual beds and red lines for unconformities). (C and F) Zoomed images of units labelled k1 and k3. From: Mangold et al., 2021.

7.5 Future prospects

During and following the currently ongoing crater floor campaign, the M2020 has great potential for making scientific observations relevant to determining the stratigraphic relations of the units in Jezero crater. There are still plenty of unit boundaries, craters, delta-associated remnant deposits to be investigated which may reveal key factors in constraining the relative timing of events in Jezero crater. Additionally, M2020 will provide the coming MSR mission with cached samples for later return to Earth. This will be of great scientific importance, as it allows us to investigate in-situ samples, giving us an abundance of scientific data that would otherwise be out of reach.

8. Conclusion

In this study, I have investigated the stratigraphic relations and origins of units present in Jezero crater using orbital data, and data from the early stages of the M2020 mission. I have made the following observations based on this data, second-order data products I made as part of the Mastcam-Z downlink science support team, as well as contributions by the rest of the Mastcam-Z team:

- The boundaries observed in my topographical map and profiles between Cf-fr and Cf-f-1 units are characterized by local topographic depressions (moats), as a result of a higher erosional rate of the relatively older Cf-f-1 unit embayed by Cf-fr. The boundaries between the Cf-fr and delta scarp/delta-associated remnant deposits are lacking moats.
- Inclination of the Cf-fr observed in my topographical profiles, is similar to the delta along axes that appear to be radial to the delta, which could indicate a shared origin, although draping of existing topography is also consistent with this sloping pattern.
- CRISM data shows clear signatures of HCP in Cf-fr, consistent with more evolved magma compositions often associated with Hesperian and Amazonian volcanics. This could suggest that the Cf-fr unit is sourced from aeolian or fluvial reworking of a regional basaltic mantling unit, resulting in fluvial deposits of basaltic composition.
- The rock morphotypes I have identified in Mastcam-Z data vary in their LCP/HCP signals. Máaz like pavers exhibit strong LCP signatures consistent with the LCP signature of the

delta fan. The two-toned massives exhibit a stronger HCP signature consistent with the Cf-fr unit.

- The origin of the delta-associated remnant deposits are, as the term suggests, related to fluvial activity forming the delta but whether they are deltaic or lacustrine deposits are unclear. The limited diversity and muteness of internal stratification in the eastern remnant complex could suggest they are lacustrine deposits rather than deltaic.
    - Kodiak is a delta remnant with exposed topsets, foresets, and bottomsets indicative of delta growth into a lake system with fluctuating lake levels.
- Various scenarios for the stratigraphic relations in Jezero crater are suggested, and my results presented in this thesis are unambiguous. Future investigations by Perseverance and the MSR mission should be sufficient to conclude on the stratigraphic relations in Jezero crater.

List of frequently used acronyms

Cf-fr	-	Crater floor fractured rough (unit)
Cf-f-1	-	Crater floor fractured 1 (unit)
Cf-f-2	-	Crater floor fractured 2 (unit)
CRISM	-	Compact Reconnaissance Imaging Spectrometer
DCS	-	Decorrelation Stretch
DEM	-	Digital Elevation Model
HCP	-	High-Calcium Pyroxene
LCP	-	Low-Calcium Pyroxene
M2020	-	Mars 2020
MEP	-	Mars Exploration Program
MER	-	Mars Exploration Rover
MRO	-	Mars Reconnaissance Orbiter
MSL	-	Mars Science Laboratory
MSR	-	Mars Sample-Return
NASA	-	National Aeronautics and Space Administration
NIR	-	Near Infrared
Us	-	Undifferentiated smooth (unit)
VNIR	-	Visible and Near Infrared

References

Allwood, Abigail C., et al. (2021) – PIXL: Planetary Instrument for X-ray Lithochemistry, Space Science Reviews, Vol. 216, Article: 134

Balaram, J., Aung, MiMi, and Golombek, Matthew P. (2021) - The Ingenuity Helicopter on the Perseverance Rover, *Space Science Reviews*, Vol. 217, Article: 56

Banerdt, Bruce W., et al. (2020) – Initial results from the InSight mission on Mars, *Nature Geoscience*, Vol. 13, pp. 183-189

Bhartia. Rohit (2021) – Perseverance's Scanning Habitable Environments with Raman and Luminescence for Organics and Chemicals (SHERLOC) Investigation, *Space Science Reviews*, Vol. 217, Article: 58

Bell III, James F., et al. (2017) – The Mars Science Laboratory *Curiosity* rover Mastcam instruments: Preflight and in-flight calibration validation, and data archiving, *Earth and Space Science*, Vol. 4, Issue 7, pp. 396-452

Bell III, James F., et al. (2021) – The Mars 2020 Perseverance Rover Mast Camera Zoom (Mastcam-Z) Multispectral, Stereoscopic Imaging Investigation, *Space Science Reviews,* Vol. 217, Article: 24

Bouvier, Laura C., et al. (2018) – Evidence for Extremely Rapid Magma Ocean Crystallization and Crust Formation on Mars, *Nature*, Vol. 558, pp. 586-589

Calef III, Fred J., et al. (2019) – Geology and origin of Taconite Crater on the Vera Rubin Ridge, In: *50th LPSC Program*

Carr, Michael H., and Head III, James W. (2009) – Geologic history of Mars, *Earth and Planetary Science Letters,* Vol. 294, pp. 185-203

Edgett, Kenneth S., and Malin, Michael C. (2014) – Heavily-cratered sedimentary rock occurrences at the surface of Mars, In: *GSA Annual Meeting in Vancouver, British Columbia Program*

Farley, Kenneth A., et al. (2020) – Mars 2020 Mission Overview, *Space Science Reviews*, Vol. 216, Article: 142

Fassett, Caleb I., and Head, James W., (2008) – Valley network-fed, open-basin lakes on Mars: Distribution and implications for Nachian surface and subsurface hydrology, *Icarus*, Vol. 198, pp. 37-56

Fassett, Caleb I., and Head, James W., (2011) – Sequence and Timing of Conditions on early Mars, *Icarus*, Vol. 211, pp. 1204-1214

Gaines, Daniel, et al. (2016) – Productivity challenges for Mars rover operations, *NASA JPL*, Planning and Robotics Workshop of ICAPS 2016

Garber, Stephen (2015) - A Chronology of Mars Exploration, *NASA History Division.* [Online] 2021 - https://history.nasa.gov/marschro.htm

Garvin, James B., and McCleese, Daniel J. (2003) – NASA's Mars Exploration Program: Scientific Strategy 1996-2020, *6th International Symposium on Mars*

Golombek, Matthew (1997) – The Mars Pathfinder Mission, *Journal of Geophysical Research*, Vol. 102, No. E2, pp. 3953-3965

Goudge, Timothy A., Mustard, John F., Head, James W., Fassett, Caleb I., and Wiseman, Sandra M. (2015) – Assessing the mineralogy of the watershed and fan deposits of the Jezero crater paleolake system, Mars, *Journal of Geophysical Research: Planets*, Vol. 120, pp. 775-808

Hamran, Svein-Erik, et al. (2020) – Radar Imager for Mars' Subsurface Experiment – RIMFAX, *Space Science Reviews,* Vol. 216, Article: 128

Harland, David (2005) – Water and the Search for Life on Mars, *Praxis Publications Inc*

Hayes, Alexander G., et al. (2021) – Pre-Flight Calibration of the Mars 2020 Rover Mastcam Zoom (Mastcam-Z) Multispectral, Stereoscopic Imager, *Space Science Reviews*, Vol. 217, Article 29

Kinch, Kjartan M., et al. (2020) – Radiometric Calibration Targets for the Mastcam-Z Camera on the Mars 2020 Rover Mission, *Space Science Reviews*, Vol. 216, Article 141

Malin, Michael C., et al. (2007) – Context Camera Investigation on board the Mars Reconnaissance Orbiter, *Journal of Geophysical Research*, Vol. 112

Mangold, Nicholas, et al. (2021) – Perseverance rover reveals an ancient delta-lake system and flood deposits at Jezero crater, Mars, *Science*

Maurice, Sylvestre, et al. (2021) – The SuperCam Instrument Suite on the Mars 2020 Rover: Science Objectives and Mast-Unit Description, *Space Science Reviews,* Vol. 217, Article: 47

McEwen, Alfred S., et al. (2007) – Mars Reconnaissance Orbiter's High Resolution Imaging Science Experiment (HiRISE), *Journal of Geophysical Research*, Vol. 112

Muirhead, Brian K., Nicholas, Austin K., Umland, Jeffrey, Sutherland, Orson, and Vijendran, Sanjay (2020) – Mars Sample Return Campaign Concept Status, *Acta Astronautica*, Vol. 176, pp 131-138

Murchie, Scott, et al. (2007) – Compact Reconnaissance Imaging Spectrometer for Mars (CRISM) on Mars Reconnaissance Orbiter (MRO), *Journal of Geophysical Research,* Vol. 112

Mustard, John F., et al. (2007) – Mineralogy of the Nili Fossae region with OMEGA/Mars Express data: 1. Ancient impact melt in the Isidis Basin and implications for the transition from the Noachian to Hesperian, *Journal of Geophysical Research*, Vol. 112

Mustard, John F., et al. (2013) – Report of the Mars 2020 Science Definition Team. [Online] 2013 - http://mepag.jpl.nasa.gov/reports/MEP/Mars_2020_SDT_Report_Final.pdf

NASA EO (2009) – The Science: Orbital Mechanics, *EOS Project Science Office* [Online] 2009 - https://earthobservatory.nasa.gov/features/OrbitsHistory/page2.php

NASA InSight (2021) – NASA's InSight Reveals the Deep Interior of Mars, *MARS InSight Mission.* [Online] 2021 - https://mars.nasa.gov/news/8996/nasas-insight-reveals-the-deep-interior-of-mars/?site=insight

NASA MER (2019) – Mars Exploration Rovers, *Mars Exploration Program & JPL.* [Online] 2021 - **https**://mars.nasa.gov/mars-exploration/missions/mars-exploration-rovers/

NASA MRO (2017) – Mars Global Coverage by Context Camera on MRO. [Online] 2021 - https://mars.nasa.gov/resources/8334/mars-global-coverage-by-context-camera-on-mro/

NASA MSL (2021) – Mars Curiosity Rover, *Mars Exploration Program & JPL.* [Online] 2021 - https://mars.nasa.gov/msl/home/

Novaković, Bojan (2008) – Senenmut: An Ancient Egyptian Astronomer, *Publication of the Astronomical Observatory of Belgrade*

Pirajno, Franco (2009) – Hydrothermal Processes Associated with Meteorite Impacts. In: Hydrothermal Processes and Mineral Systems. *Springer*, pp. 1097-1126

Rodriguez-Manfredi, José A. (2021) – The Mars Environmental Dynamics Analyzer, MEDA. A suite of environmental sensors for the Mars 2020 mission, *Space Science Reviews,* Vol. 217, Article: 48

Ruff, Steve W. (2017) – Investigating the floor of paleolake Jezero by way of Gusev crater, *Fourth Conference on Early Mars*, LPI Contrib. No. 2014

Schon, Samuel C., Head, James W., and Fassett, Caleb I. (2012) – An overfilled lacustrine system and progradational delta in Jezero crater, Mars: Implications for Noachian climate, *Planetary and Space Science,* Vol. 67, pp. 28-45

Shotwell, Robert (2005) – Phoenix – the first Mars Scout mission, *Acta Astronautica,* Vol. 57, pp. 121-134

Stack, M. Kathryn, et al. (2020) – Photogeologic Map of the Perseverance Rover Field Site in Jezero Crater Constructed by the Mars 2020 Science Team, *Space Science Reviews,* Vol. 216, Article: 127

Welch, Richard, Limonadi, Daniel, and Manning, Robert (2013) – Systems engineering the Curiosity Rover: A retrospective, *8th International Conference on System of Systems Engineering,* pp. 70-75

Westman, Robert S. (2001) – Kepler's Early Physical-Astrological Problematic, *Journal for the History of Astronomy*, Vol. 32, pp. 227-236

Williford, Kenneth H., et al. (2020) – The NASA Mars 2020 Rover Mission and the Search for Extraterrestrial Life, In: From Habitability to Life on Mars, *Elsevier*, pp. 275-308

Zurek, Richard W., and Smrekar, Suzanne E. (2007) – An overview of the Mars Reconnaissance Orbiter (MRO) science mission, *Journal of Geophysical Research*, Vol. 112